PROPOSAL AND ANALYSIS OF A NON-COLLINEAR WAVE MIXING TECHNIQUE FOR THE DETECTION OF MICRO-CRACKS USING PHASED ARRAYS

A Thesis
Presented to
The Academic Faculty

By

Max Philipp May

In Partial Fulfillment
of the Requirements for the Degree
Master of Science in Engineering Science and Mechanics in the
School of Civil and Environmental Engineering

Georgia Institute of Technology

December 2020

PROPOSAL AND ANALYSIS OF A NON-COLLINEAR WAVE MIXING TECHNIQUE FOR THE DETECTION OF MICRO-CRACKS USING PHASED ARRAYS

Approved by:

Professor Laurence J. Jacobs, Advisor
School of Civil and Environmental Engineering
Georgia Institute of Technology

Dr. Jin-Yeon Kim
School of Civil and Environmental Engineering
Georgia Institute of Technology

Dr. Christine Valle
School of Mechanical Engineering
Georgia Institute of Technology

Date Approved: August 11, 2020

ACKNOWLEDGEMENTS

First, I would like to thank my advisor Prof. Laurence Jacobs for his guidance and help during my research. His decades of experience helped a lot and he was always able to motivate me during our discussions. He gave me the freedom to choose what the focus of my studies should be and was responsible for the organization of the program at Georgia Tech.

Second, I have to say thanks to Dr. Jin-Yeon Kim for his valuable advice concerning different topics in the field of non destructive evaluation. Despite the unfavorable circumstances during a global pandemic, he found ways to support me throughout the course of my research and took the time to explain the subtleties of wave propagation and its nonlinear aspects to me.

Third, I want to thank Prof. Michael Hanss, Dominik Hose and Sibylle Langer at the University of Stuttgart for making this program possible. Thanks for selecting me for the program and organizing everything on the German part of this prolific academic exchange. You are keeping this program alive throughout the years and helped me to prepare all documents for my studies at Georgia Tech.

Fourth, I want to thank my parents back home and all friends in Germany and new ones in the US for all the good times and supporting me with their kindness during this year of excitement and surprises.

Last but not least, I thank my significant other Anne-Marie for her love, all the good time in Canada and the hour long video calls during these distancing times.

TABLE OF CONTENTS

LIST OF TABLES

LIST OF FIGURES

LIST OF SYMBOLS

Symbol	Description
B_0	Reference configuration
B_t	Current configuration
t	Time
X	Lagrangian coordinate description
x	Eulerian coordinate description
$\boldsymbol{F}$	Deformation gradient
$\boldsymbol{E}$	Lagrangian strain tensor
$\boldsymbol{P}$	First Piola-Kirchhoff tensor
$\boldsymbol{u}$	Displacement vector
Grad/grad	Gradient with respect to Lagrangian/Eulerian description
Div/div	Divergence with respect to Lagrangian/Eulerian description
δ_{ij}	Kronecker delta
W	Strain energy density function
C_{ijkl}	Second order elastic constants
C_{ijklmn}	Third order elastic constants
σ	Cauchy stress tensor
λ, μ	Lamé constants
l, m, n	Murnaghan constants
A, B, C	Landau and Lifshitz constants
t_i	Traction vector
$\hat{\boldsymbol{n}}$	Unit normal vector
V	Volume

table continues

continue table

Symbol	Description
A	Surface
ρ	Density
$\boldsymbol{U}$	Amplitude vector
$\hat{\boldsymbol{U}}$	Unit amplitude vector
$\boldsymbol{k}$	Wave vector
$\hat{\boldsymbol{k}}$	Unit wave vector
k	Wave number
ω	Angular frequency
f	Frequency
c_L,c_T	Longitudinal and transverse wave velocity
$c = c_T/c_L$	Wave velocity ratio
$\Delta\theta$	Mixing angle
θ_s	Steering angle
x_m, y_m	Mixing point coordinates
λ_l	Wavelength
n_c	Number of wave cycles
$A^{(i)}$	Aperture size
$a = \omega_2/\omega_1$	Frequency ratio for mixing
r, r_1, r_2	Resonant and incident wave path lengths
δT_i	Delay for i-th element
δ_x	Element pitch
δ_e	Element size
N	Number of array elements

table continues

continue table

Symbol	Description
y_f	Focusing distance
β_L, β_T, β_{rel}	Longitudinal, transversal and relative acoustic nonlinearity parameter
p	Pressure
A, A_0	Attenuated and initial amplitude
α_0, α_{0L}, α_{0T}	Material attenuation coefficient
η_m, η_g	Material and geometric attenuation parameter
$\bullet_{att}$	Attenuated value
U_0^+	Resonant amplitude from attenuated incident waves
Att_{rel}	Relative path attenuation
$\bullet_{meas}$	Simulated value to be measured
$\bullet_{comp}$	Value approx. compensated for sensitivity
$\bullet_{comp.exact}$	Value exactly compensated for sensitivity
$\bullet_{max}$	Maximum value
ASR	Alcali-silica reaction
FMC	Full matrix capture
L	Longitudinal wave
NDE	Non-destructive evaluation
PLL	Phase Locked Loop
SV, SH	Vertical and horizontal polarized shear wave
TOE	Third order elastic constants
TFM	Total focusing method
NLU	Nonlinear ultrasound

SUMMARY

In this thesis, a new ultrasonic measurement setup for the detection of micro-scale damage in cement based materials is proposed and analyzed. The idea is to use the nonlinear phenomenon of wave mixing to characterize third order elastic behavior of a material. By wave mixing, the nonlinear interaction between two ultrasound waves creating a third resonant wave inside a material is meant. The amplitude of this third wave is dependent on the third order nonlinear constants of a material, which in turn are influenced by micro-scale damage inside the material structure. Furthermore, a nonlinear technique is especially needed in the case of attenuative materials, which prevent the use of higher frequencies to get good resolution with linear approaches. Recent measurement results using a wave mixing technique are designed in a fixed setup to evalute a single point inside the material or scan line regions by moving the ultrasonic equipment. This limitation originates from the use of common ultrasonic transducer elements generating an ultrasound wave at a fixed angle by using the refraction of wedges. As a remedy to this limitation, phased arrays can be used as a source for the incident waves instead. Thus, having the advantage to change the beam angle without changing the physical measurement configuration. Two phased arrays are used on one side of the specimen to generate incident shear waves. If the the beams intersect inside the material at a point fulfilling certain mixing conditions, a longitudinal resonant wave is generated which amplitude is proportional to the amount of nonlinearity inherent to the mixing volume. This resonant wave can be measured by a receiver on the other side of the material to asses, e.g., micro-crack density in the mixing volume.

In this thesis, necessary and sufficient conditions for this non-collinear shear wave mixing are derived. Furthermore, the basic laws for beam steering with phased arrays are explained and the mixing volume is modeled. Finally, advantages and limitations of this measurement technique as well as design specifics for the practical construction of a measurement setup are discussed.

CHAPTER 1
INTRODUCTION

1.1 Motivation

Detecting distributions of micro-cracks in cement based materials is important for life-time prediction of structures. Achieving this task with ultrasonic testing through linear ultrasonic techniques is hindered by resolution limits determined by the wavelength, with shorter wavelengths exhibiting higher attenuation of waves in concrete materials, as well as scattering effects. Different research [1–3] identifies especially small defects, detectable through the quadratic nonlinear response, relevant for early detection of fatigue and dislocation damage. Whereas larger cracks, detectable by linear methods, appear more close to the end of the lifespan of structures.

Another problem, is the ability to systematically scan a volume of a large structure in a short time. This is hard to achieve by single transducer methods, which involve time consuming precise movements of the ultrasound equipment around multiple locations. In the recent years, measurement techniques using phased arrays instead of single transducer elements are gaining more and more attention, as the equipment gets more affordable and they find their way into industrial applications. An ultrasonic array consists of multiple transducers, which can be separately controlled for firing ultrasonic pulses at different instances in time to generate an arbitrary pressure field. This gives them the advantage to conduct different measurements without changing the measurement setup, such as beam steering and beam focusing or combinations thereof [4]. Full matrix capture (FMC) in combination with the Total Focusing Method (TFM) [5] is one of the most popular techniques in the latest research, representing the current benchmark standard regarding the imaging resolution among linear techniques using phased arrays. In order to gather information about finer

structural defects and their location, nonlinear techniques can be employed [6].

1.2 Goals

In this thesis, a measurement technique using non-collinear shear wave mixing to measure the nonlinearity at different points in a cement based structure is proposed. Two phased arrays are used to create coplanar shear wave beams at an angle, which cross inside the specimen in an interaction volume. Under certain conditions (frequency of incident waves and angles) a resonant wave is generated, due to the nonlinearity of the material. This phenomenon was first described by G.L. Jones and D.R. Kobett in [7] and experimentally verified by F.R. Rollins [8]. The ratio of the resonant wave amplitude to the incident wave amplitudes can be used as a relative measure of nonlinearity inside the material called the relative acoustic nonlinearity parameter β_{rel}. For the purpose of these measurements, a setup with two phased arrays on one side of the material and an air coupled, movable receiving transducer on the other side is analyzed. Thus, giving the advantage to use beam steering with the arrays, in order to scan different points, as opposed to an approach using single transducers on wedges, which have to be moved in order to scan points along a line.

It was shown [9, 10], that the nonlinear property of the material changes at the locations with higher micro-crack density, which are filled with air or gel. This provides an indirect measure to find aggregations of cracks and can serve as an indicator for the lifetime prediction of a material.

1.3 Thesis outline

In Chapter 2, the basic constitutive equations for nonlinear elasticity and the nonlinear wave equation are derived. This is continued by an explanation of the wave mixing phenomenon as a possible solution to the nonlinear wave equation and stating the general necessary and sufficient conditions for the occurrence of a resonant or scattered wave. To conclude, related work in the field of wave mixing for non-destructive evaluation (NDE) is presented.

In Chapter 3, the proposed measurement setup is introduced. The equations from chapter 2 are used to derive the relevant equations for the here presented application. Furthermore, the use of wave pulses with a finite amount of cycles instead of continuous wave beams is modeled. To conclude, a short summary on work related to the modeling of cracks and an overview of different acoustic nonlinearity parameters is given.

In Chapter 4 simulative results are used to analyze different aspects to be considered for this approach.

Finally, Chapter 5 concludes the analysis of the presented measurement technique and points out open questions and future work of interest.

CHAPTER 2
THEORETHICAL BACKGROUND

In this chapter, an overview of the necessary background theory for the described application is given. For further reading on nonlinear elasticity the books [11, 12] are recommended. The effect of nonlinearity on wave propagation is discussed in [13–15].

2.1 Nonlinear elasticity

In order to describe the nonlinear phenomena and derive the respective equations for the measuring methods used in this thesis, a background in nonlinear elasticity is mandatory. The here used derivation partly follows [13]. First, the basic continuum mechanical notation to describe all particles is introduced. In Figure 2.1 the reference B_0 and deformed B_t state of a continuum is shown. The distinction betwen capital letters for the Lagrangian and lower case letters for Eulerian description is important. $\boldsymbol{X}$ describes a unique label for a particle in the reference configuration (also called Lagrangian description), whereas the lower case letter $\boldsymbol{x}$ describes a position in the deformed configuration (also called Eulerian description). This also defines the frames to which derivatives refer, e.g., 'Grad' for gradient in Lagrangian and 'grad' for gradient in Eulerian coordinates. These two description are mapped by a function

$$\boldsymbol{x} = \boldsymbol{\chi}(\boldsymbol{X}, t). \tag{2.1}$$

The deformation gradient is defined as

$$\boldsymbol{F} = \frac{\partial \boldsymbol{\chi}(\boldsymbol{X}, t)}{\partial \boldsymbol{X}} = \text{Grad}\boldsymbol{\chi}(\boldsymbol{X}, t). \tag{2.2}$$

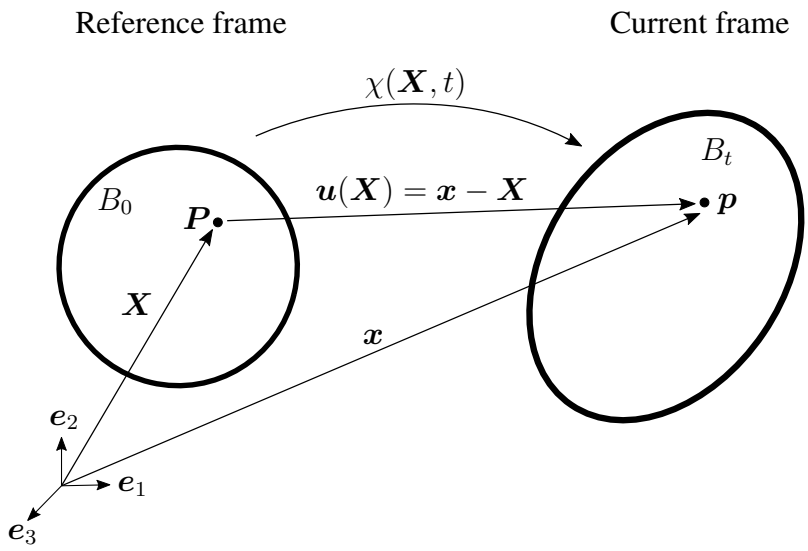

Figure 2.1: Reference and current configuration of a continuum.

The displacement of a particle can be written as

$$\boldsymbol{u} = \boldsymbol{x} - \boldsymbol{X} = \boldsymbol{\chi}(\boldsymbol{X}, t) - \boldsymbol{X} \tag{2.3}$$

with which equation (2.2) can be rewritten as

$$F_{ij} = \frac{\partial u_i}{\partial X_j} + \delta_{ij}, \tag{2.4}$$

where $i, j = \{1, 2, 3\}$ to express all quantities in indicial notation and

$$\delta_{ij} = \begin{cases} 1, & \text{for i=j} \\ 0, & \text{else} \end{cases} \tag{2.5}$$

denotes the Kronecker delta. An introduction to the index notation can be found in [14, 16] or many other common books on continuum mechanics. In the following, index notation is used where it is beneficial for the understanding and summation over repeated indices according to the Einstein summation convention is implied. Further, the strain tensor in

Lagrangian description is defined as

$$E_{ij} := \frac{1}{2}(F_{ki}F_{kj} - \delta_{ij}). \tag{2.6}$$

Using equation (2.4) in equation (2.6) leads to

$$\begin{aligned} E_{ij} &= \frac{1}{2}\left(\frac{\partial u_i}{\partial X_j} + \frac{\partial u_j}{\partial X_i} + \frac{\partial u_m}{\partial X_i}\frac{\partial u_m}{\partial X_j}\right) \\ &\approx \frac{1}{2}\left(\frac{\partial u_i}{\partial X_j} + \frac{\partial u_j}{\partial X_i}\right), \end{aligned} \tag{2.7}$$

which is the well known expression for the Green/Engineering-strain in the Lagrangian form, when neglecting the quadratic term for small displacements $\boldsymbol{u}$.

Nonlinear elasticity can be seen from an energy standpoint of view by stating the strain energy density function as a Taylor series approximation

$$W \approx C_0 + C_{ij}E_{ij} + \frac{1}{2!}C_{ijkl}E_{ij}E_{kl} + \frac{1}{3!}C_{ijklmn}E_{ij}E_{kl}E_{mn} + \ldots, \tag{2.8}$$

with coefficients $C_0 = 0$ and $C_{ij} = 0$, to get 0 energy and a minimum at $E_{ij} = 0$, thus resulting in a typical positive definite energy function. To establish a constitutive relationship, the first Piola-Kirchhoff stress tensor is introduced and has the following definition in terms of the strain energy density function

$$\boldsymbol{P} = \boldsymbol{F}\left(\frac{\partial W(\boldsymbol{E})}{\partial \boldsymbol{E}}\right)^T. \tag{2.9}$$

The Piola-Kirchhoff stress is used, because it is a two-point tensor relating forces in the current configuration to surface areas in the reference configuration. Similarly $\boldsymbol{F}$ is a two point tensor relating Lagrangian and Eulerian quantities, whereas the commonly known Cauchy stress tensor is an Eulerian description with surface areas in the B_t configuration.

Furthermore, the Cauchy stress has the relationship

$$\boldsymbol{\sigma} = \frac{1}{\det(\boldsymbol{F})} \boldsymbol{F}\boldsymbol{P}^T \tag{2.10}$$

to the first Piola-Kirchhoff stress. For further derivations only two-point tensors are used and all spatial derivatives can be carried out in the Lagrangian coordinates. Plugging equation (2.8) in equation (2.9) and carrying out the derivative, then using equations (2.4) and (2.7) to get the stress tensor dependent on displacement only, leads to

$$P_{ij} \approx C_{ijkl} \frac{\partial u_k}{\partial X_l} + \frac{1}{2} M_{ijklmn} \frac{\partial u_k}{\partial X_l} \frac{\partial u_m}{\partial X_n} + \ldots, \tag{2.11}$$

where C_{ijkl} is the usual stiffness tensor comprised of the second order elastic constants and

$$M_{ijklmn} = C_{ijklmn} + C_{ijln}\delta_{km} + C_{jnkl}\delta_{im} + C_{jlmn}\delta_{ik}, \tag{2.12}$$

with C_{ijklmn} comprised of the third order elastic constants (TOE). The entries of the fourth order tensor C_{ijkl} can be reduced to 21 by using the symmetries

$$C_{ijkl} = C_{jikl} = C_{ijlk}, \tag{2.13}$$

$$C_{ijkl} = C_{klij}, \tag{2.14}$$

which result from the symmetry of the strain tensor $E_{ij} = E_{ji}$ in equation (2.6) and the fact that the strain energy density equation (2.8) is scalar valued. A similar argument can be made for the TOE C_{ijklmn}. In the course of the here presented application, the inspected solid is assumed to be isotropic. Isotropy means that the elastic properties of a solid are independent of its orientation. This leads to simplified expressions for the tensors in equa-

Table 2.1: Relationship between Murnaghan constants and elastic parameters by Landau and Lifshitz.

Murnaghan	$l = B + C$	$m = A/2 + B$	$n = A$
Landau & Lifshitz	$A = n$	$B = m - n/2$	$C = l - m + n/2$

tion (2.11)

$$
\begin{aligned}
C_{ijkl} &= \lambda\delta_{ij}\delta_{kl} + \mu(\delta_{ik}\delta_{jl} + \delta_{il}\delta_{jk}),\\
C_{ijklmn} &= 2(l - m + n/2)\delta_{ij}\delta_{kl}\delta_{mn}\\
&\quad + 2(m - n/2)(\delta_{ij}I_{klmn} + \delta_{kl}I_{mnij} + \delta_{mn}I_{ijkl})\\
&\quad + n/2(\delta_{ik}I_{jlmn} + \delta_{il}I_{jkmn} + \delta_{jk}I_{ilmn} + \delta_{jl}I_{ikmn}),\\
I_{ijkl} &= \frac{1}{2}(\delta_{ik}\delta_{jl} + \delta_{il}\delta_{jk}),
\end{aligned}
\tag{2.15}
$$

with Lamé parameters λ and μ and Murnaghan constants l, m and n introduced by Murnaghan in [12]. In literature, it is also common to express the TOE in terms of elastic constants A, B and C introduced by Landau and Lifshitz in [11]. The relationship between these elastic parameters is shown in table 2.1.

2.2 The nonlinear wave equation

The basic law of the motion of particles in continuum mechanics, often called Newton's second law, is the balance of linear momentum

$$
\int_{B_0} \rho\dot{\boldsymbol{\chi}}(\boldsymbol{X}, t)d\boldsymbol{V} = \int_{\partial B_0} \boldsymbol{P}\hat{\boldsymbol{n}}d\boldsymbol{A} + \int_{B_0} \boldsymbol{b}_0 d\boldsymbol{V}. \tag{2.16}
$$

Here the term on the left hand side is the change in linear momentum with density ρ, the first term on the right hand side is the integral of surface forces with unit normal $\hat{\boldsymbol{n}}$ of the surface considered and the second term on the right hand side represents the integral over the gravitational body forces $\boldsymbol{b}_0$ per unit volume. In this case all integrals are computed in Lagrangian coordinates $\boldsymbol{X}$, however the resulting forces and change in linear momentum

is in the current configuration due to the use of two-point tensors. By the use of Gauss's divergence theorem, the surface force term in equation (2.16) can be rewritten as a volume integral of the stress divergence

$$\int_{B_0} \rho \ddot{\boldsymbol{\chi}}(\boldsymbol{X}, t) d\boldsymbol{V} = \int_{B_0} \text{Div}(\boldsymbol{P}) d\boldsymbol{V} + \int_{B_0} \boldsymbol{b}_0 d\boldsymbol{V}. \tag{2.17}$$

Equation (2.17) holds true for all subsets of the body B_0, therefore

$$\begin{aligned} &\int_{B_0} \Big(\rho \ddot{\boldsymbol{\chi}}(\boldsymbol{X}, t) - \text{Div}(\boldsymbol{P}) - \boldsymbol{b}_0 \Big) d\boldsymbol{V} = 0 \\ &\Rightarrow \rho \ddot{\boldsymbol{\chi}}(\boldsymbol{X}, t) = \text{Div}(\boldsymbol{P}) + \boldsymbol{b}_0 \end{aligned} \tag{2.18}$$

which is called the equilibrium equation in continuum mechanics. For the considered application with wave propagation in solid materials, gravitational body forces can be neglected. Furthermore, the time derivative of the mapping function $\boldsymbol{\chi}$ can be expressed in terms of displacement as

$$\frac{\partial^2 \boldsymbol{u}}{\partial t^2} = \frac{\partial^2 \Big(\boldsymbol{\chi}(\boldsymbol{X}, t) - \boldsymbol{X} \Big)}{\partial t^2} = \ddot{\boldsymbol{\chi}}(\boldsymbol{X}, t). \tag{2.19}$$

Using equation (2.19) and the expression from equation (2.11) for the first Piola-Kirchhoff stress tensor and assuming isotropy as in equation (2.15), equation (2.18) becomes

$$\underbrace{\rho \frac{\partial^2 u_i}{\partial t^2} - \mu \frac{\partial^2 u_i}{\partial X_k \partial X_k} - (\lambda + \mu) \frac{\partial^2 u_l}{\partial X_l \partial X_i}}_{L_i(\boldsymbol{u})} = G_i(\boldsymbol{u}), \tag{2.20}$$

with

$$
\begin{aligned}
G_i(\boldsymbol{u}) = &\left(\mu + \frac{n}{4}\right)\left(\frac{\partial^2 u_l}{\partial X_k \partial X_k}\frac{\partial u_l}{\partial X_i} + \frac{\partial^2 u_l}{\partial X_k \partial X_k}\frac{\partial u_i}{\partial X_l} + 2\frac{\partial^2 u_i}{\partial X_l \partial X_k}\frac{\partial u_l}{\partial X_k}\right) \\
&+ \left(\lambda + \mu + m - \frac{n}{4}\right)\left(\frac{\partial^2 u_l}{\partial X_i \partial X_k}\frac{\partial u_l}{\partial X_k} + \frac{\partial^2 u_k}{\partial X_l \partial X_k}\frac{\partial u_i}{\partial X_l}\right) \\
&+ \left(\lambda + m - \frac{n}{2}\right)\left(\frac{\partial^2 u_i}{\partial X_k \partial X_k}\frac{\partial u_l}{\partial X_l}\right) \\
&+ \left(m - \frac{n}{4}\right)\left(\frac{\partial^2 u_k}{\partial X_l \partial X_k}\frac{\partial u_l}{\partial X_i} + \frac{\partial^2 u_l}{\partial X_i \partial X_k}\frac{\partial u_k}{\partial X_l}\right) \\
&+ (2l - m + \frac{n}{2})\left(\frac{\partial^2 u_k}{\partial X_i \partial X_k}\frac{\partial u_l}{\partial X_l}\right).
\end{aligned}
\tag{2.21}
$$

This is the nonlinear wave equation used in [7, 17] to derive the solution for second order nonlinear interaction of plane waves, also called wave mixing. For $G_i(\boldsymbol{u}) = 0$ equation (2.20) is the well-known linear homogeneous wave equation.

2.3 Wave mixing

In the case of a linear systems the superposition principle is one of the most important concepts, allowing linear combination of solutions to a differential equation to be solutions themselves. For the case of linear elasticity, two ultrasound waves would propagate through a solid without interacting with each other and the solution would be a linear superposition of both waves. However, when considering nonlinear elastic properties of a material, different types of self and cross interaction between the two waves can occur. These interactions were first described by G.L. Jones and D.R. Kobett [7] and experimentally validated by F.R. Rollins [8]. In order to find a solution for equation (2.20) the solution is considered to consist of two parts

$$
\boldsymbol{u} = \boldsymbol{u}^{(h)} + \boldsymbol{u}^{(p)}, \tag{2.22}
$$

with $\boldsymbol{u}^{(h)}$ being a solution to the linear homogeneous wave equation and $\boldsymbol{u}^{(p)}$ being a small perturbation ($\|\boldsymbol{u}^{(p)}\| \ll \|\boldsymbol{u}^{(h)}\|$) as a correction to fulfill equation (2.20) for $G_i(\boldsymbol{u}) \neq 0$. As the interaction of two monochromatic incident waves is of interest

$$\boldsymbol{u}^{(h)}(\boldsymbol{X}, t) = \boldsymbol{U}^{(1)} \cos(\omega_1 t - \boldsymbol{k}^{(1)} \cdot \boldsymbol{X}) + \boldsymbol{U}^{(2)} \cos(\omega_2 t - \boldsymbol{k}^{(2)} \cdot \boldsymbol{X}), \tag{2.23}$$

with angular frequencies ω_1, ω_2 of the incident waves is considered as a solution to the homogeneous wave equation $L_i(\boldsymbol{u}^{(h)}) = 0$. With wave amplitudes

$$\boldsymbol{U}^{(1)} = U^{(1)}\hat{\boldsymbol{U}}^{(1)}, \quad \boldsymbol{U}^{(2)} = U^{(2)}\hat{\boldsymbol{U}}^{(2)}, \tag{2.24}$$

where $U^{(1)}, U^{(2)}$ are the absolute values and $\hat{\boldsymbol{U}}^{(1)}, \hat{\boldsymbol{U}}^{(2)}$ are the unit vectors in the direction of the wave amplitudes. And wave vectors

$$\boldsymbol{k}^{(1)} = k^{(1)}\hat{\boldsymbol{k}}^{(1)}, \quad \boldsymbol{k}^{(2)} = k^{(2)}\hat{\boldsymbol{k}}^{(2)}, \tag{2.25}$$

where $k^{(1)} = \omega_1/c_{l/t}, k^{(2)} = \omega_2/c_{L/T}$ are the wavenumbers ($c_{L/T}$ to be replaced by the respective wave velocity) and $\hat{\boldsymbol{k}}^{(1)}, \hat{\boldsymbol{k}}^{(2)}$ are the unit vectors in the propagation directions. A sketch of all relevant quantities is shown in figure 2.2. Using the ansatz from equation (2.22) in equation (2.20) results in

$$\begin{aligned} L_i(\boldsymbol{u}^{(h)} + \boldsymbol{u}^{(p)}) &= G_i(\boldsymbol{u}^{(h)} + \boldsymbol{u}^{(p)}) \\ \Leftrightarrow L_i(\boldsymbol{u}^{(h)}) + L_i(\boldsymbol{u}^{(p)}) &= G_i(\boldsymbol{u}^{(h)}) + G_i(\boldsymbol{u}^{(p)}), \end{aligned} \tag{2.26}$$

with $L_i(\boldsymbol{u}^{(h)}) = 0$ by definition as it is a solution to the homogeneous equation, and $G_i(\boldsymbol{u}^{(p)}) \approx 0$ as $\boldsymbol{u}^{(p)}$ is considered small and can be neglected for quadratic and higher

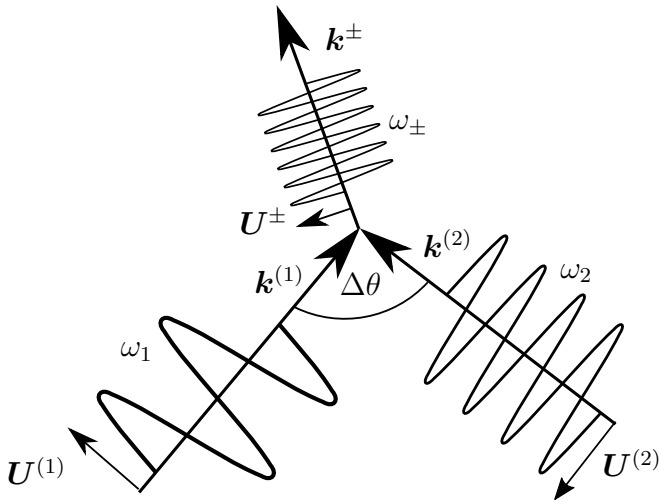

Figure 2.2: Mixing of two incident waves, with frequencies $\omega_1, \omega_2, \omega_{\pm}$, wave vectors $\boldsymbol{k}^{(1)}, \boldsymbol{k}^{(2)}, \boldsymbol{k}^{\pm}$, displacement vectors $\boldsymbol{U}^{(1)}, \boldsymbol{U}^{(2)}, \boldsymbol{U}^{\pm}$ and mixing angle $\Delta\theta$.

order terms. Thus, the problem can be stated as an inhomogeneous linear wave equation

$$L_i(\boldsymbol{u}^{(p)}) = \rho \frac{\partial^2 u_i^{(p)}}{\partial t^2} - \mu \frac{\partial^2 u_i^{(p)}}{\partial X_k \partial X_k} - (\lambda + \mu) \frac{\partial^2 u_l^{(p)}}{\partial X_l \partial X_i} = G_i(\boldsymbol{u}^{(h)}), \tag{2.27}$$

with

$$\begin{aligned} G_i(\boldsymbol{u}^{(h)}) =& b_i^+ \sin(\omega_+ t - \boldsymbol{k}^+ \cdot \boldsymbol{X}) \\ &+ b_i^- \sin(\omega_- t - \boldsymbol{k}^- \cdot \boldsymbol{X}) \end{aligned} \tag{2.28}$$

as the excitation term on the right hand side, consisting of two harmonic terms, with

$$\begin{aligned} \omega_+ = \omega_1 + \omega_2, \quad \omega_- = \omega_1 - \omega_2 \\ \boldsymbol{k}^+ = \boldsymbol{k}^{(1)} + \boldsymbol{k}^{(2)}, \quad \boldsymbol{k}^- = \boldsymbol{k}^{(1)} - \boldsymbol{k}^{(2)}. \end{aligned} \tag{2.29}$$

The amplitudes for this generative term are computed in [7] as

$$\begin{aligned}
\boldsymbol{b}^{\pm} = -\frac{U^{(1)}U^{(2)}}{2}\Bigg[&(\mu+\frac{n}{4})\Big\{(\hat{\boldsymbol{U}}^{(1)}\cdot\hat{\boldsymbol{U}}^{(2)})(\boldsymbol{k}^{(2)}\cdot\boldsymbol{k}^{(2)})\boldsymbol{k}^{(1)} \pm (\hat{\boldsymbol{U}}^{(1)}\cdot\hat{\boldsymbol{U}}^{(2)})(\boldsymbol{k}^{(1)}\cdot\boldsymbol{k}^{(1)})\boldsymbol{k}^{(2)} \\
&+(\hat{\boldsymbol{U}}^{(2)}\cdot\boldsymbol{k}^{(1)})(\boldsymbol{k}^{(2)}\cdot\boldsymbol{k}^{(2)})\hat{\boldsymbol{U}}^{(1)} \pm (\hat{\boldsymbol{U}}^{(1)}\cdot\boldsymbol{k}^{(2)})(\boldsymbol{k}^{(1)}\cdot\boldsymbol{k}^{(1)})\hat{\boldsymbol{U}}^{(2)} \\
&\pm 2(\hat{\boldsymbol{U}}^{(2)}\cdot\boldsymbol{k}^{(1)})(\boldsymbol{k}^{(1)}\cdot\boldsymbol{k}^{(2)})\hat{\boldsymbol{U}}^{(1)} + 2(\hat{\boldsymbol{U}}^{(1)}\cdot\boldsymbol{k}^{(2)})(\boldsymbol{k}^{(1)}\cdot\boldsymbol{k}^{(2)})\hat{\boldsymbol{U}}^{(2)}\Big\} \\
(\lambda+\mu-\frac{n}{4}+m)&\Big\{\pm(\hat{\boldsymbol{U}}^{(1)}\cdot\hat{\boldsymbol{U}}^{(2)})(\boldsymbol{k}^{(1)}\cdot\boldsymbol{k}^{(2)})\boldsymbol{k}^{(1)} + (\hat{\boldsymbol{U}}^{(1)}\cdot\hat{\boldsymbol{U}}^{(2)})(\boldsymbol{k}^{(1)}\cdot\boldsymbol{k}^{(2)})\boldsymbol{k}^{(2)} \\
&+(\hat{\boldsymbol{U}}^{(2)}\cdot\boldsymbol{k}^{(2)})(\boldsymbol{k}^{(1)}\cdot\boldsymbol{k}^{(2)})\hat{\boldsymbol{U}}^{(1)} \pm (\hat{\boldsymbol{U}}^{(1)}\cdot\boldsymbol{k}^{(1)})(\boldsymbol{k}^{(1)}\cdot\boldsymbol{k}^{(2)})\hat{\boldsymbol{U}}^{(2)}\Big\} \\
(\lambda-\frac{n}{2}+m)&\Big\{\pm(\hat{\boldsymbol{U}}^{(2)}\cdot\boldsymbol{k}^{(2)})(\boldsymbol{k}^{(1)}\cdot\boldsymbol{k}^{(1)})\hat{\boldsymbol{U}}^{(1)} + (\hat{\boldsymbol{U}}^{(1)}\cdot\boldsymbol{k}^{(1)})(\boldsymbol{k}^{(2)}\cdot\boldsymbol{k}^{(2)})\hat{\boldsymbol{U}}^{(2)}\Big\} \\
(m-\frac{n}{4})&\Big\{(\hat{\boldsymbol{U}}^{(2)}\cdot\boldsymbol{k}^{(2)})(\hat{\boldsymbol{U}}^{(1)}\cdot\boldsymbol{k}^{(2)})\boldsymbol{k}^{(1)} \pm (\hat{\boldsymbol{U}}^{(2)}\cdot\boldsymbol{k}^{(1)})(\hat{\boldsymbol{U}}^{(1)}\cdot\boldsymbol{k}^{(1)})\boldsymbol{k}^{(2)} \\
&\pm(\hat{\boldsymbol{U}}^{(1)}\cdot\boldsymbol{k}^{(2)})(\hat{\boldsymbol{U}}^{(2)}\cdot\boldsymbol{k}^{(1)})\boldsymbol{k}^{(1)} + (\hat{\boldsymbol{U}}^{(1)}\cdot\boldsymbol{k}^{(2)})(\hat{\boldsymbol{U}}^{(2)}\cdot\boldsymbol{k}^{(1)})\boldsymbol{k}^{(2)}\Big\} \\
(2l-m+\frac{n}{2})&\Big\{\pm(\hat{\boldsymbol{U}}^{(1)}\cdot\boldsymbol{k}^{(1)})(\hat{\boldsymbol{U}}^{(2)}\cdot\boldsymbol{k}^{(2)})\boldsymbol{k}^{(1)} + (\hat{\boldsymbol{U}}^{(1)}\cdot\boldsymbol{k}^{(1)})(\hat{\boldsymbol{U}}^{(2)}\cdot\boldsymbol{k}^{(2)})\boldsymbol{k}^{(2)}\Big\}\Bigg],
\end{aligned} \tag{2.30}$$

where the $(\lambda - \frac{n}{2} + m)$-term has been added for completeness, which characterizes self interactions of the primary waves. Equation (2.30) can be noticeably reduced to a smaller number of terms for the consideration of single cases, as presented later in section 3.1 for two shear incident waves. A possible solution, which fulfills equation (2.27) is

$$u_i^{(p)} = a_i^{+}\sin(\omega_{+}t - k_j^{+}X_j) + a_i^{-}\sin(\omega_{-}t - k_j^{-}X_j), \tag{2.31}$$

where $a_i^{\pm}$ are amplitude vectors dependent on the specified right hand side $b_i^{\pm}$. For simplicity, the interaction of two incidence waves can always be observed in the 2D ($i = \{1, 2\}$) plane formed by their respective propagation direction vectors $\hat{\boldsymbol{k}}^{(1)}$ and $\hat{\boldsymbol{k}}^{(2)}$. This makes the derivation of the necessary and sufficient frequency and angle conditions for wave mixing simpler without loss of generality. Using equation (2.31) in equation (2.27) and calculating

the time and spatial derivatives leads to a linear system of equations

$$\rho \underbrace{\begin{bmatrix} d_1^{\pm} & s^{\pm} \\ s^{\pm} & d_2^{\pm} \end{bmatrix}}_{=\boldsymbol{A}^{\pm}} \boldsymbol{a}^{\pm} = \boldsymbol{b}^{\pm}, \tag{2.32}$$

with

$$\begin{aligned} d_1^{\pm} &= -\omega_{\pm}^2 + c_L^2 k_1^{\pm 2} + c_T^2 k_2^{\pm 2}, \\ d_2^{\pm} &= -\omega_{\pm}^2 + c_L^2 k_2^{\pm 2} + c_T^2 k_1^{\pm 2}, \\ s^{\pm} &= (c_L^2 - c_T^2) k_1^{\pm} k_2^{\pm}. \end{aligned} \tag{2.33}$$

In order to produce a resonance wave, the solution of equation (2.32) must not exist and the form in equation (2.31) no longer applies. Instead, the amplitude of the solution is proportional to the size of the interaction volume, which gives rise to the name resonance or scattered wave. The sufficient and necessary conditions resulting from equation (2.32) are

$$\det(\boldsymbol{A}^{+}) = 0 \quad \text{or} \quad \det(\boldsymbol{A}^{-}) = 0, \tag{2.34}$$

with

$$\det(\boldsymbol{A}^{\pm}) = c_L^2 c_T^2 \left(k_j^{\pm} k_j^{\pm} - \frac{\omega_{\pm}}{c_L^2} \right) \left(k_j^{\pm} k_j^{\pm} - \frac{\omega_{\pm}}{c_T^2} \right) \tag{2.35}$$

and

$$\text{rank}(\boldsymbol{A}^{+}|\boldsymbol{b}^{+}) \neq \text{rank}(\boldsymbol{A}^{+}) \quad \text{or} \quad \text{rank}(\boldsymbol{A}^{-}|\boldsymbol{b}^{-}) \neq \text{rank}(\boldsymbol{A}^{-}) \tag{2.36}$$

respectively. Where equation (2.35) means that there is no trivial solution to equation (2.32) and equation (2.36) additionaly ensures that $\boldsymbol{b}^{\pm}$ is not in the span of $\boldsymbol{A}^{\pm}$. These conditions

were first derived in [18] to be applied on 1D wave mixing. Additionally, equation (2.34) resembles the condition

$$\frac{\omega_{\pm}}{c_{L/T}}\hat{\boldsymbol{n}} - \boldsymbol{k}^{\pm} = 0 \tag{2.37}$$

mentioned in [7]. Meaning, for a resonance solution to exist, there has to be one unit normal vector $\hat{\boldsymbol{n}}$, such that equation (2.37) is fulfilled. Here c_L or c_T and $\boldsymbol{k}^+$ or $\boldsymbol{k}^-$ has to be chosen according to the expected resonant wave. From the absolute value of equation (2.37) a condition for the angle between the incident waves

$$\begin{aligned}
\left(\frac{\omega_1 \pm \omega_2}{c^{(r)}}\right)^2 &= \|\boldsymbol{k}^{(1)} \pm \boldsymbol{k}^{(2)}\| \\
&= {k^{(1)}}^2 + {k^{(2)}}^2 \pm 2(\boldsymbol{k}^{(1)} \cdot \boldsymbol{k}^{(2)}) \\
&= \frac{{\omega_1}^2}{{c^{(1)}}^2} + \frac{{\omega_2}^2}{{c^{(2)}}^2} \pm 2\frac{\omega_1\omega_2}{c^{(1)}c^{(2)}}\cos(\Delta\theta) \\
\Leftrightarrow \cos(\Delta\theta) &= \mp\frac{1}{2}\left[\frac{c^{(2)}}{c^{(1)}}\frac{1}{a} + \frac{c^{(1)}}{c^{(2)}}a - \frac{c^{(1)}c^{(2)}}{{c^{(r)}}^2}\left(\frac{1}{a} + a \pm 2\right)\right]
\end{aligned} \tag{2.38}$$

is formulated. Here $a = \omega_2/\omega_1$ as the frequency ratio, $\Delta\theta$ as the angle between the wave vectors and $c^{(1)}, c^{(2)}, c^{(r)}$ have to be replaced by the respective incident and considered resonant wave velocities for the used material (same notation as in figure 2.2). In addition, this gives a condition on the range of the frequency ratio a as $-1 < \cos(\Delta\theta) < 1$. This is summarized in table 2.2 adopted from Jones [7], which states the respective angle and frequency conditions. By specifying the type of incident waves, longitudinal or shear, and for shear waves the type of polarization, horizontal or vertical, the coefficients in equation (2.30) can be calculated and equation (2.27) can be solved in the individual cases. In general, 54 different interactions with different types of waves can be considered, however only 10 of them lead to physically possible results as presented in table 2.3 which is adopted from [17]. The seminal paper by Jones and Kobbet [7] considered all of the eight noncollinear interactions. However, the polarization of the shear waves is not specified in

Table 2.2: Resonance conditions for non-collinear interaction of different wave types, adopted from [7] with $a = \omega_2/\omega_1$ and $c = c_T/c_L$.

Primary waves	Resonant wave type and frequency	Direction of scattered wave	$\cos(\Delta\theta)$	Frequency limits
$T(\omega_1) - T(\omega_2)$	$L(\omega_+)$	$\boldsymbol{k}^+$	$c^2 + [(c^2-1)(a^2+1)/2a]$	$\frac{1-c}{1+c} < a < \frac{1+c}{1-c}$
$L(\omega_1) - L(\omega_2)$	$T(\omega_-)$	$\boldsymbol{k}^-$	$1/c^2 + [(c^2-1)(a^2+1)/2ac^2]$	$\frac{1-c}{1+c} < a < \frac{1+c}{1-c}$
$L(\omega_1) - T(\omega_2)$	$L(\omega_+)$	$\boldsymbol{k}^+$	$c + [a(c^2-1)/2c]$	$0 < a < \frac{2c}{1-c}$
$L(\omega_1) - T(\omega_2)$	$L(\omega_-)$	$\boldsymbol{k}^-$	$c + [a(1-c^2)/2c]$	$0 < a < \frac{2c}{1+c}$
$L(\omega_1) - T(\omega_2)$	$T(\omega_-)$	$\boldsymbol{k}^-$	$1/c + [(c^2-1)/2ac]$	$\frac{1-c}{2} < a < \frac{1+c}{2}$

Table 2.3: Possible resonant wave interactions, adopted from [17]. For x (interaction for a certain range of angles), $\bar{\text{x}}$ (interaction for a certain range of angles and antilinear) and $=$ (collinear), interaction is possible. For O (due to polarization) and ' ' space (due to no feasible resonance condition solution), no interaction is possible.

		Resonant wave					
		$\omega_r = \omega_1 + \omega_2$			$\omega_r = \omega_1 - \omega_2$		
N	Incidence waves	L	SV	SH	L	SV	SH
1	$L(\omega_1)$ and $L(\omega_2)$	$=$			$=$	$\bar{\text{x}}$	O
2	$L(\omega_1)$ and $SV(\omega_2)$	$\bar{\text{x}}$			x	$\bar{\text{x}}$	O
3	$SV(\omega_1)$ and $L(\omega_2)$	x					
4	$SV(\omega_1)$ and $SV(\omega_2)$	$\bar{\text{x}}$	O	O		O	O
5	$SH(\omega_1)$ and $SH(\omega_2)$	$\bar{\text{x}}$	O	O		O	O
6	$L(\omega_1)$ and $SH(\omega_2)$	O			O	O	$\bar{\text{x}}$
7	$SH(\omega_1)$ and $L(\omega_2)$	O					
8	$SH(\omega_1)$ and $SV(\omega_2)$	O	O	O		O	O
9	$SV(\omega_1)$ and $SH(\omega_2)$	O	O	O		O	O

the particular cases in table 2.2, as the respective conditions stay the same while the amplitude of the scattered wave changes for different polarization combinations or may be zero.

2.4 Related work

Over the course of the past decade, numerous applications of nonlinear wave mixing in non destructive evaluation (NDE) have been described. Its main feature is given by the fact, that micro cracks and other fatigue damage influences the quadratic nonlinearity of a material, which can be measured spatially discretized through wave mixing techniques.

One application is the measurement of nonlinearity associated with deformation, plasticity and fatigue. Liu *et al.* [19] demonstrated the measurment of an acoustic nonlinearity parameter and its correlation with the deformation of A1-6061 alloys. In [20], the viability of detecting plasticity and fatigue damage by non-collinear wave mixing was investigated by Croxford *et al.*. Furthermore, Sun *et al.* [21] used non-collinear shear wave mixing for the detection of plasticity and analyzed the sensitivity of the procedure on the incidence angles.

Another application is the assessment at interfaces and bonds. Ju *et al.* [22] used a nonlinear wave mixing technique to inspect adhesive joints for thermal aging after they considered one-way mixing for the inspection of an adhesive layer [23]. In addition, Zhang *et al.* [24, 25] used non-collinear mixing of shear incidence waves at an interface to evaluate bond quality between solids.

The main application in this thesis is the detection of micro-cracks, which is also extensively discussed in the literature. Blanloeuil *et al.* [10] analyzed the detection of closed cracks with non-collinear mixing by means of a FEM simulation. More lately, Zhao *et al.* [9] used one-way collinear wave mixing for the detection and characterization of micro-cracks.

These approaches for the detection of micro scale damage have the advantage of lo-

calizing the damage within the structure by means of the mixing zone, compared to older nonlinear NDE techniques [26] gathering only limited spatial information. However, using fixed positions for single transducers results in a limited number of points to be scanned. A possible remedy is the precise movement of the ultrasonic equipment, but this can be time consuming. Therefore, in this work an analysis of the use of wave mixing techniques in combination with phased array transducers is presented. Phased arrays consist of many single transducer elements and can be purchased in different spatial and technical configurations. Their main advantage is the possibility to create a beam at a programmable angle, without using a wedge, through the use of firing delays between the single transducer elements. Thus, a region of points can be scanned for a fixed positioning of two arrays in less time. A review on phased arrays is given by Drinkwater and Wilcox in [4], in section 3.2 the basic delay laws will be introduced and in section 4.1 their capabilities and limitations for the considered application will be discussed.

CHAPTER 3

TECHNICAL APPROACH

In this chapter, the technical details of the planned application are dicussed. The goal is to propose a design for a setup to scan a specimen for micro-cracks. A sketch of the proposed measurement setup is shown in figure 3.1. Two phased arrays are used on one side of the specimen to generate incident shear waves at the desired angles. Each array is put on a wedge to produce an angle offset of $52.7°$ from the vertical beam direction. Thus, smaller steering angles can be used for the region of interest, which is a result discussed in section 4.1. The two wave beams intersect under the mixing angle $\Delta\theta$ at the interaction volume of which nonlinearity is ought to be measured. All angles for a set mixing point can be calculated for a fixed distance L of the arrays as

$$\theta_s^{(1)} = \tan\left(\frac{y_m}{x_m}\right), \theta_s^{(2)} = \tan\left(\frac{y_m}{L - x_m}\right), \Delta\theta = 180° - \theta_s^{(1)} - \theta_s^{(2)}, \tag{3.1}$$

with mixing point position (x_m, y_m). In this thesis, the distance between the arrays is set to $L = 1\mathrm{m}$ in order for the scanning region to fit for a $40\mathrm{cm}$ thick specimen. However, L can be chosen according to the thickness of any specimen without changing the quality of the general results presented herein. When the required frequency ratio conditions for the current mixing angle are met, resonance inside the interaction volume creates a scattered wave. The amplitude of this scattered wave is proportional to the nonlinearty of the material inside the interaction volume depicted in red in figure 3.1 and then can be measured by an air coupled receiver on the opposite side of the specimen. This process is repeated for multiple points inside the specimen, thereby a scan of a larger volume measuring its nonlinear behavior is conducted. This is potentially much faster than conventional techniques, which require the movement of all transducers or a more restricted scanning area, e.g., a

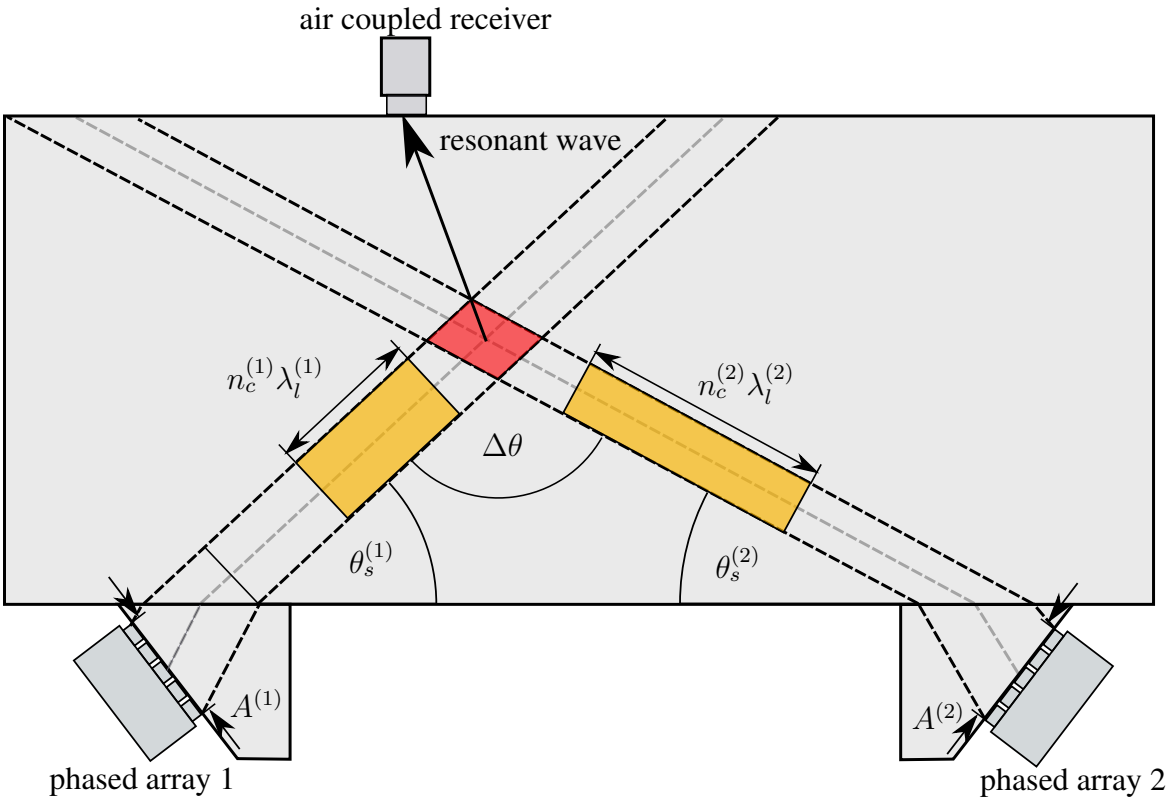

Figure 3.1: Sketch of setup for wave mixing with two phased arrays. With wave pulses in yellow, maximum possible interaction volume in red and depiction of steering angles $\theta_s^{(1)}, \theta_s^{(2)}$, array apertures $A^{(1)}, A^{(2)}$, wavelengths $\lambda_l^{(1)}, \lambda_l^{(2)}$, number of cycles $n_c^{(1)}, n_c^{(2)}$ and mixing angle $\Delta\theta$.

line. However, this only gives a relative measure of nonlinearity for one point compared to others inside the volume and usually the measured amplitude values are normalized by a constant, e.g., the maximum measured amplitude for the scanned volume. In order to get absolute values, it would be necessary to precisely know all displacement amplitudes, which would require precise calibration of the transducers with expensive equipment and exact modeling of the transducer characteristics transforming voltage into displacement. Nonetheless, the proposed measurement techniques allows the detection of micro-crack aggregations, because a higher density of micro-cracks leads to a greater amount of nonlinearity relative to other points with less micro-cracks. The values can also be compared to an intact specimen of the same composition. Thus, no knowledge of absolute measurement of nonlinearty, for example in the form of Murnaghan constants is required. Another

advantage of this technique is the spatial information provided by this kind of measurement, as the measured amplitude is only dependent on the nonlinearity of the interaction volume and mostly independent of nonlinearities on the propagation paths to and from the interaction volume.

In the following sections different aspects of this measurement technique will be discussed in detail. In Section 3.1, the necessary and sufficient conditions on the mixing angles and frequency ratio for the generation of a resonant wave, using two shear incident waves, are derived. Furthermore, formulas for the computation of the resonant wave amplitudes are derived and the sensitivity for the two possible types of polarization on the nonlinearity is analyzed. In Section 3.2, the basic functionality of phased arrays, as well as beam steering and beam focusing is explained. In Section 3.3, the difference between the use of continuous waves and the use of wave pulses with a limited number of cycles is discussed. Thus leading, to a model of the interaction volume used for the simulations in chapter 4. Finally, Section 3.4 discusses the modeling of cracks in literature and different acoustic nonlinearity parameters commonly used to quantify nonlinearity.

3.1 Wave mixing of two oblique angle shear waves

Two oblique angle shear waves are used as incident waves, which have better resolution due to the smaller wavelength compared to longitudinal waves with the same frequency. Furthermore, they have to be used in interaction case 4 and 5 of table 2.3 for non-collinear mixing producing a longitudinal resonant wave. In order to avoid high attenuation, lower frequencies are preferred. The used frequency range is approximately $20\mathrm{kHz}$ to $100\mathrm{kHz}$. From table 2.2 or equation (2.38) the respective angle condition is

$$\cos(\Delta\theta) = \frac{c_T^2}{c_L^2} + \frac{1}{2}\left(\frac{c_T^2}{c_L^2} - 1\right)\left(\frac{\omega_1}{\omega_2} + \frac{\omega_2}{\omega_1}\right). \tag{3.2}$$

Table 3.1: Typical values for material parameters of concrete based on measurements in [27, 28], mortar based on [29] and pore free cement paste based on [30].

Medium	λ [GPa]	μ [GPa]	l [GPa]	m [GPa]	n [GPa]	ρ [kg m^{-3}]	c_L [mm µs^{-1}]	c_T [mm µs^{-1}]
Concrete	12.68	17.52	-3007	-2283	-1813	2400	4.459	2.702
Mortar	9.31	8.59	-	-	-	2018	3.623	2.063
Cement paste	42	21	-	-	-	2660	5.620	2.810

For $-1 < \cos(\Delta\theta) < 1$, equation (3.2) has only one meaningful root leading to the frequency range

$$\frac{1 - c_T/c_L}{1 + c_T/c_L} < \frac{\omega_1}{\omega_2} < \frac{1 + c_T/c_L}{1 - c_T/c_L} \Leftrightarrow \frac{1 - c_T/c_L}{1 + c_T/c_L} < \frac{\omega_2}{\omega_1} < \frac{1 + c_T/c_L}{1 - c_T/c_L}. \tag{3.3}$$

Typical material parameters for cement based materials are listed in table 3.1. Cement based materials already have an inherent nonlinearity in the intact state due to their heterogeneity. However, the TOE for an intact specimen are only listed for concrete, because they are hard to measure precisely and there are only a few measurements in cement based material of these parameters in recent research [28]. Nevertheless, the trends and behavior in the following analysis holds true for all kinds of materials, only the absolute values (dependent on the actual Murnaghan constants) would change. For concrete the frequency ratio range for wave mixing is

$$0.2454 < \frac{\omega_2}{\omega_1} < 4.0751 \tag{3.4}$$

,for mortar and cement paste it is

$$0.2744 < \frac{\omega_2}{\omega_1} < 3.6449 \text{ and } \frac{1}{3} < \frac{\omega_2}{\omega_1} < 3 \tag{3.5}$$

respectively. The achievable mixing angles for this range of frequency ratios can be computed by equation (3.2) and are shown in figure 3.2. One can see, that the range of mixing

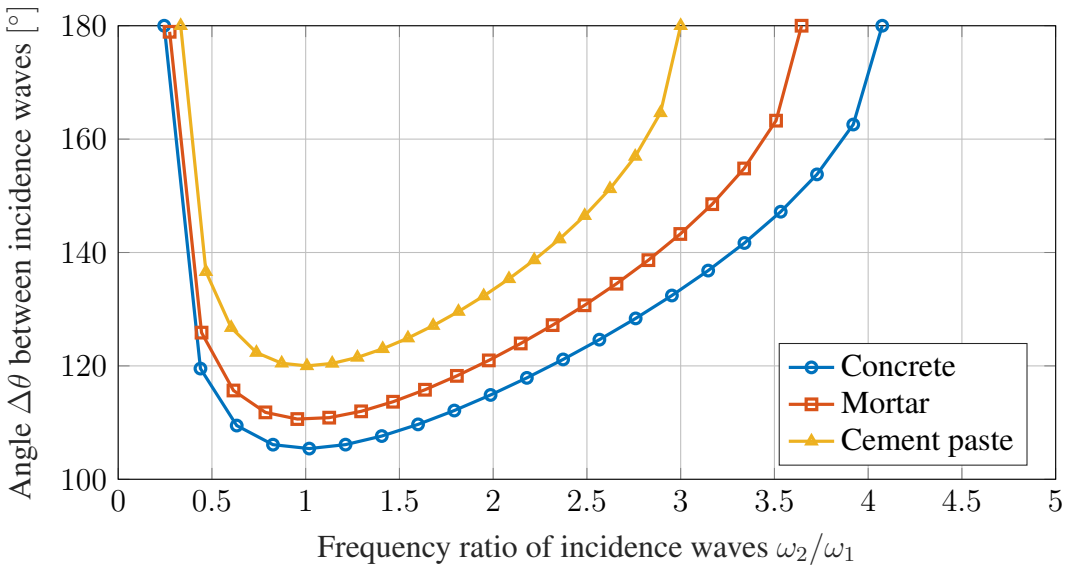

Figure 3.2: Mixing angle over frequency ratio according to mixing condition for two incidence shear waves in concrete, mortar and cement paste.

angles $\Delta\theta$ is similar for all materials, but the frequency ratio, defined as $a = \omega_2/\omega_1$, for a specific $\Delta\theta$ is different as the velocity ratio, defined as $c = c_T/c_L$, is different for every material. A minimum angle in concrete is reached for a ratio of 1 at $105.4°$. The upper limit is $180°$, but this is further limited by the maximum feasible steering angle of the used arrays which will be discussed in section 3.2. Actually, the mixing conditions below $a = 1$ describe the same cases as the ratios $a > 1$, because for two exactly identical generated incident waves it is a matter of definition if $\omega_1 > \omega_2$ or $\omega_2 > \omega_1$ in the fraction for the frequency ratio depending on which incident wave is declared number one. This is also the reason for the equivalence in equation (3.3) and why the lower limit is always the reciprocal of the upper limit. Therefore, we define $a = \omega_2/\omega_1$ with $\omega_2 > \omega_1$ in all cases and look only at ratios $a > 1$.

Similar to the case of Thales's theorem, where for a right triangle the third point lies on the circumference of a circle, there are certain lines corresponding to an arbitrary constant third angle of the triangle. As an illustration, some of these lines, in the range of the required mixing angles, are shown in figure 3.3. Inspired from the ancient Greek, these lines can be called isogonics. This means for the presented application, that all points

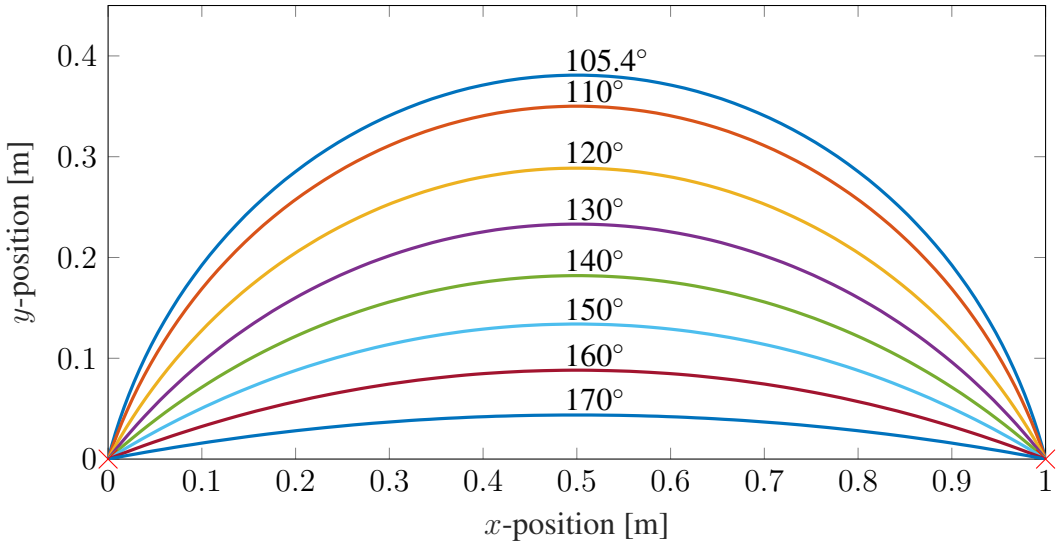

Figure 3.3: Lines of all points with the same mixing angle (Isogonics) for 1 m distance between arrays. From $105.4°$ to $170°$ which would be limited by the maximum steering angle of the arrays.

laying on the same isogonic can be scanned with the same mixing angle between the two shear incident wave. With lines closer to the lower surface corresponding to higher angles. For this range of mixing angles the steering angles of the incident waves are in the range from $\theta_s^{(i)} = 0°$ to $\theta_s^{(i)} = 180° - 105.4° = 74.6°$. Wedges are used to get an angle offset of $90° - (180° - 105.4°)/2 = 52.7°$ for a steering angle of $0°$ of the arrays measured from a vertical line. This leads to better spatial isolated measurements and higher intensity inside the mixing volume, because smaller array steering angles lead to smaller beam widths and better beam directivity which is discussed in section 4.1.

Until now the polarization of the two incidence shear waves was not considered. There are two possible cases. They can be polarized in the plane formed by their wave vectors $\boldsymbol{k}^{(1)}, \boldsymbol{k}^{(2)}$ (case 5 table 2.3) or both pointing in the same direction orthogonal to this plane (case 4 table 2.3). Each case results in a different amplitude of the resonant wave. The general expression for the amplitude of the resonance wave, when two shear incident wave

produce a longitudinal wave with sum frequency ω_+, can be found in [7] as

$$\boldsymbol{U}^+ = \frac{(\boldsymbol{b}^+ \cdot \hat{\boldsymbol{k}}^+)}{4\pi c_L^2 \rho r} V \hat{\boldsymbol{k}}^+, \tag{3.6}$$

with r as the distance to the measurement point from the center of the interaction volume V.

For the in plane polarization the geometric relations

$$\begin{aligned}
\boldsymbol{k}^{(1)} \cdot \boldsymbol{k}^{(1)} = \frac{\omega_1^2}{c_T^2}, \quad \boldsymbol{k}^{(2)} \cdot \boldsymbol{k}^{(2)} = \frac{\omega_2^2}{c_T^2}, \quad \boldsymbol{k}^{(1)} \cdot \boldsymbol{k}^{(2)} = \frac{\omega_1 \omega_2}{c_T^2} \cos(\Delta\theta), \\
\hat{\boldsymbol{U}}^{(1)} \cdot \hat{\boldsymbol{U}}^{(1)} = 1, \quad \hat{\boldsymbol{U}}^{(2)} \cdot \hat{\boldsymbol{U}}^{(2)} = 1, \quad \hat{\boldsymbol{U}}^{(1)} \cdot \hat{\boldsymbol{U}}^{(2)} = \cos(\Delta\theta), \\
\hat{\boldsymbol{U}}^{(1)} \cdot \boldsymbol{k}^{(1)} = 0, \quad \hat{\boldsymbol{U}}^{(2)} \cdot \boldsymbol{k}^{(2)} = 0, \\
\hat{\boldsymbol{U}}^{(1)} \cdot \boldsymbol{k}^{(2)} = \frac{\omega_2}{c_T} \cos(\Delta\theta + \pi/2), \quad \hat{\boldsymbol{U}}^{(2)} \cdot \boldsymbol{k}^{(1)} = \frac{\omega_1}{c_T} \cos(\Delta\theta - \pi/2), \\
\boldsymbol{k}^{(2)} = \begin{bmatrix} \cos(\Delta\theta) & \sin(\Delta\theta) \\ -\sin(\Delta\theta) & \cos(\Delta\theta) \end{bmatrix} \boldsymbol{k}^{(1)}, \quad \boldsymbol{U}^{(2)} = \begin{bmatrix} \sin(\Delta\theta) & -\cos(\Delta\theta) \\ \cos(\Delta\theta) & \sin(\Delta\theta) \end{bmatrix} \boldsymbol{k}^{(1)}, \\
\boldsymbol{U}^{(1)} = \begin{bmatrix} 0 & -1 \\ 1 & 0 \end{bmatrix} \boldsymbol{k}^{(1)}
\end{aligned} \tag{3.7}$$

can be used in equation (2.30). Resulting in the right hand side

$$\boldsymbol{b}^+ = -\frac{U^{(1)} U^{(2)} \omega_1 \omega_2}{4 c_T^2} [\lambda + \mu + \cos(2\Delta\theta)(\lambda + 3\mu + 2m)] \boldsymbol{k}^+. \tag{3.8}$$

Equation (3.8) is plugged in equation (3.6) and equation (3.2) is used to express everything dependent on the frequency ratio $a = \omega_2/\omega_1$ to get

$$\begin{aligned}
U^+ = -\frac{U^{(1)} U^{(2)} \omega_1^3 V}{16\pi r \rho} \frac{1}{c_L^3 c_T^2} \Bigg[(\lambda + 2\mu) \Big\{ (1 - c^2)(a + a^2) \Big\} \\
+ (\lambda + 3\mu + 2m) \Big\{ 2 \Big((a + \frac{1}{a}) \frac{c^2 - 1}{2} + c^2 \Big)^2 - 1 \Big\} \Bigg],
\end{aligned} \tag{3.9}$$

with $c = c_T/c_L$.

For the out of plane polarized shear waves the following geometries change

$$\begin{gathered}\hat{\boldsymbol{U}}^{(1)} \cdot \hat{\boldsymbol{U}}^{(2)} = 1, \quad \hat{\boldsymbol{U}}^{(1)} \cdot \boldsymbol{k}^{(2)} = 0, \quad \hat{\boldsymbol{U}}^{(2)} \cdot \boldsymbol{k}^{(1)} = 0, \\ \boldsymbol{U}^{(1)} = \begin{bmatrix} 0 \\ 0 \\ 1 \end{bmatrix} U^{(1)}, \quad \boldsymbol{U}^{(2)} = \begin{bmatrix} 0 \\ 0 \\ 1 \end{bmatrix} U^{(2)}.\end{gathered} \tag{3.10}$$

Following along the same lines as for the in plane polarized shear waves results in

$$\boldsymbol{b}^{+} = -\frac{U^{(1)}U^{(2)}}{2c_T^2}\left[(\mu + \frac{n}{4})(\omega_2^2\boldsymbol{k}^{(1)} + \omega_1^2\boldsymbol{k}^{(2)}) + (\lambda + \mu - \frac{n}{4} + m)\omega_1\omega_2\cos(\Delta\theta)\boldsymbol{k}^{+}\right] \tag{3.11}$$

and

$$\begin{aligned}U^{+} = &-\frac{U^{(1)}U^{(2)}\omega_1^3 V}{16\pi r\rho}\frac{1}{c_T^4 c_L}\left[(\mu + \frac{n}{4})\left\{(a^3+1)(c^2-1) + a(a+1)(c^2+1)\right\}\right. \\ &\left. + (\lambda + \mu - \frac{n}{4} + m)\left\{c^2(3c^2-1)(a+a^2) + c^2(c^2-1)(a^3+1)\right\}\right].\end{aligned} \tag{3.12}$$

Because the resonant wave amplitudes equations (3.9) and (3.12) are dependent on the Murnaghan constants m or m and n respectively, it is possible to measure the difference in nonlinearity between different volumes inside a specimen. Thereby, identifying regions with micro-crack damage, which changes the nonlinear behavior of the material region. Previous research concerned with the feasibility of nonlinearity measurements to asses structure damage is discussed in section 3.4. In Figure 3.4, the normalized absolute value of the resonant wave amplitudes over the product of the incident wave amplitudes, for both polarization cases in concrete is shown. This result shows, how the resonant wave amplitude for measuring nonlinearity changes based on the mixing angle and the polarization of the incident waves. Mortar and cement paste have qualitatively similar amplitude dependence and

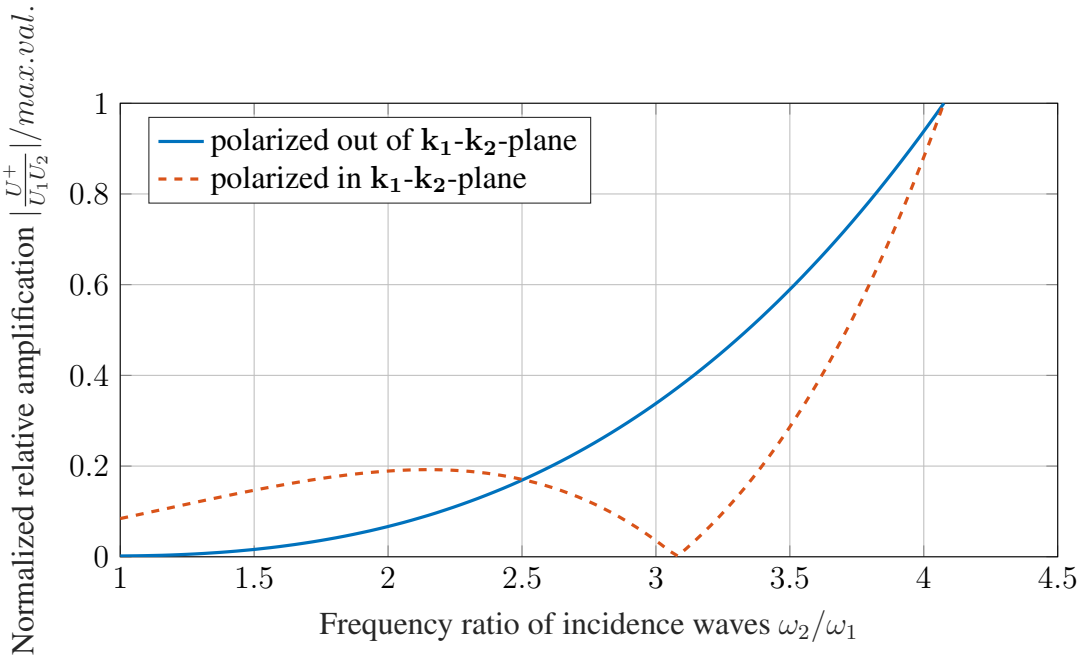

Figure 3.4: Relative amplification for different frequency ratios in concrete, normalized by maximum value.

similar curves for different types of wave mixing interactions were numerically calculated in [17] for polyvinyl chloride (PVC). For the in plane polarization, a minimum is reached at $a = 3.07$, which is actually a sign switch causing a $180°$ phase shift, if not considering the absolute amplitude value. This is due to the $2\cos(\Delta\theta)^2 - 1$ term, with the cosine replaced by equation (3.2) in equation (3.9). For $\Delta\theta > 135°$ the $(\lambda + 3\mu + 2m)$ term starts to cancel out the $(\lambda + \mu)$ term and then the expression in equation (3.9) swaps its sign. Using out of plane polarized shear waves the sensitivity increases monotonically, has no extra minimum and is bigger in the region $a > 2.5$. Whereas, in plane polarization gives better results in the region $a < 2.5$. However, for out plane polarized shear waves, either (s-wave) transducers or a setup with two angled wedge interfaces in combination with a longitudinal wave (p-wave) transducer are needed. Therefore, it is advantageous that the proposed setup (with two shear wave transducer phased arrays) permits both polarization configurations.

A special case of non-collinear shear wave mixing is the antilinear case with $\Delta\theta =$

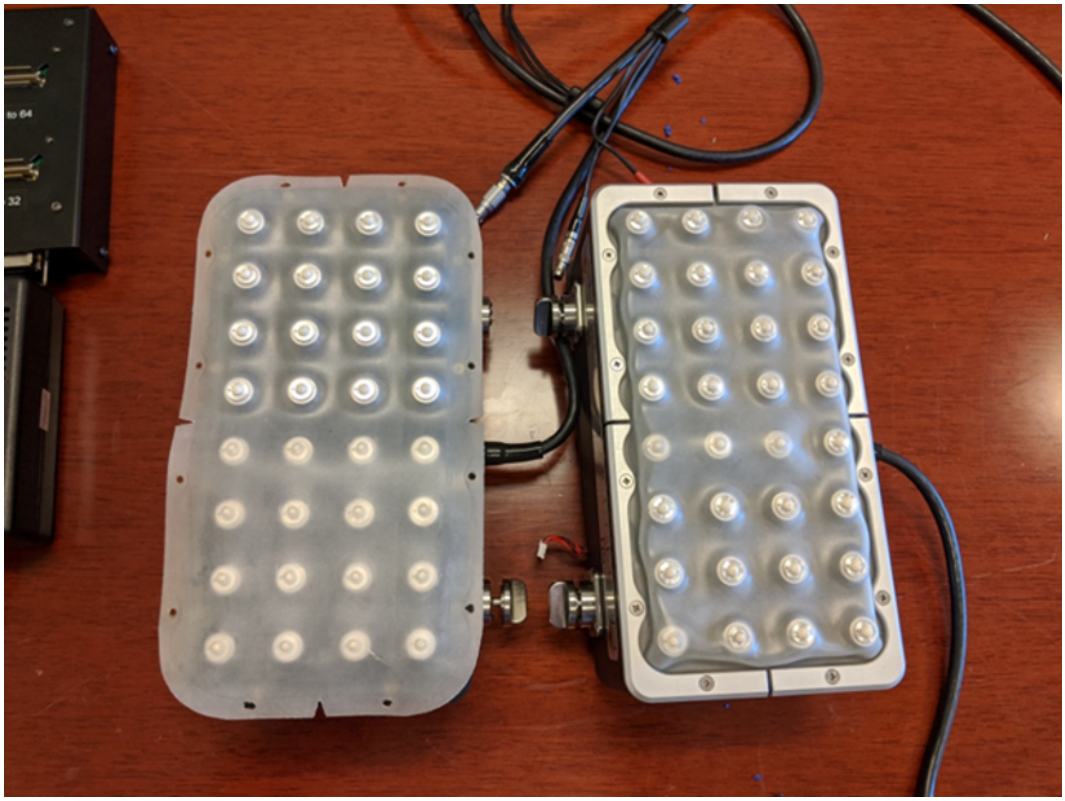

Figure 3.5: Ultrasonic phased array with shear wave transducers (ceramic tips) for concrete inspection.

$180°$, which is indicated by the bar above the 'x' in cases 4 and 5 of table 2.3. At this point, both amplitudes reach their maximum for $a = 4.0751$, which can be seen in figure 3.4. Both curves were normalized by the same maximum value so the amplitudes match. Effectively both polarization cases collapse into the same type of interaction in the antilinear case. Here, the polarization does not matter as long as both incident waves are polarized in the same plane, thus giving the same resonant wave amplitude.

3.2 Phased arrays

Phased arrays are made of multiple single element ultrasonic transducer positioned with a fixed pitch in between. They give the possibility to generate an arbitrary ultrasonic field, but are also used to reproduce fields of traditional single element transducer configurations. In Figure 3.5 a 32 element shear wave array for concrete inspection is shown. For this work,

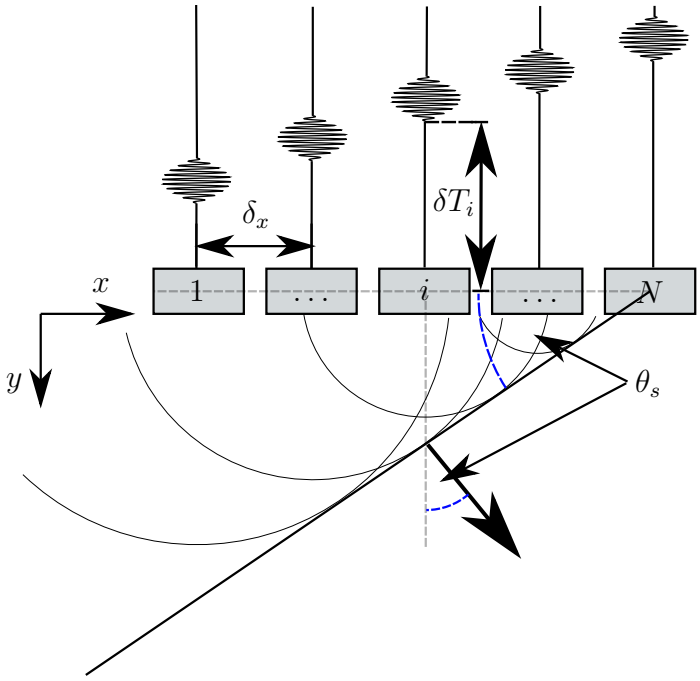

Figure 3.6: Illustration of beam steering with steering angle θ_s, element spacing δ_x, firing delay δT_i and elements 1 to N from left to right.

beam steering is the most relevant delay law for the generation of a plane incident wave steered in a desired direction to replace the use of common single element transducers generating a wave front at a fixed angle. Additionally, beam focusing is explained for completeness, which could be used in future work for further improvement of the presented technique.

For beam steering, the delay between the firing of the different transducers is used to get a phase difference between the waves emitted by the transducers, which in superposition creates a wave front at an angle. This is illustrated in figure 3.6. The time delay δT_i for the i-th element from left to right can be calculated as

$$\delta T_i = i\delta_x \sin(\theta_s)/c_{L/T}, \tag{3.13}$$

with δ_x as the pitch between elements, θ_s as the steering angle and $c_{L/T}$ as the respective wave velocity.

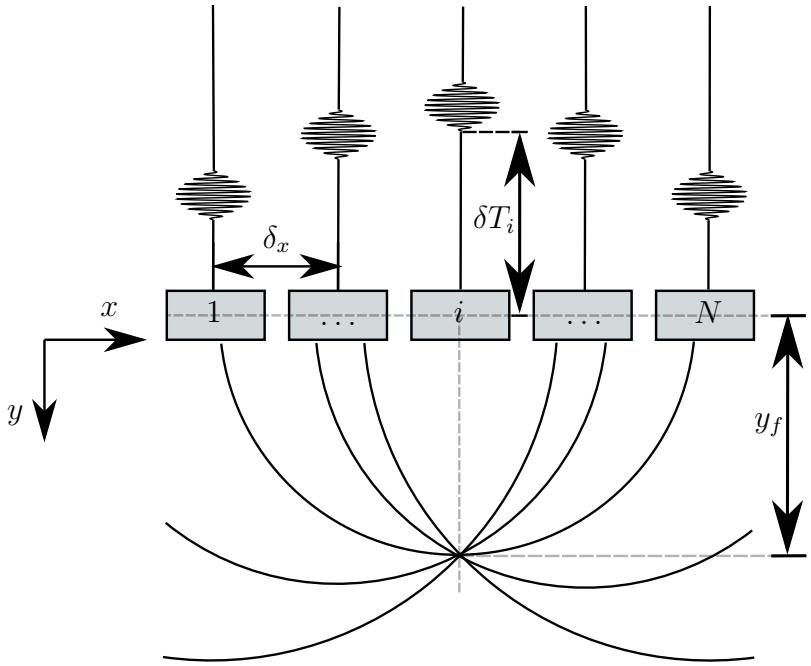

Figure 3.7: Illustration of beam focusing with focus point at depth y_f, element spacing δ_x, firing delay δT_i and elements 1 to N from left to right.

Beam focusing uses the same principle, but the result of the superposition is a constructive sum of all wave amplitudes at a specific point, illustrated in figure 3.7. The time delay δT_i for the i-th element can be calculated as

$$\begin{aligned} \delta T_i &= \left(y_f - \sqrt{(i\delta_x - (N-1)\delta_x/2)^2 + y_f^2} \right) / c_{L/T} - t_{min}, \\ t_{min} &= \min_i \left(y_f - \sqrt{(i\delta_x - (N-1)\delta_x/2)^2 + y_f^2} \right) / c_{L/T}, \end{aligned} \tag{3.14}$$

with y_f as the focusing depth and t_{min} as the time to shift the delays by the maximum negative delay value to get $\delta T_i > 0$.

Beam steering and focusing can be combined by adding the delays to get a resulting wave steered and focused at any point. Beam steering suffices for the basic task to generate incidence waves at an arbitrary angle for mixing at a desired location inside the specimen. Combination with beam focusing could be used in future work to improve resolution and intensity by the creation of a smaller interaction volume. But the analysis is much more complicated in this case, as the assumption of plane wave fronts for the analytical solution

is not fulfilled anymore. This could be further investigated by FEM analysis.

3.3 Wave mixing of pulses

Until now, a fixed volume of interaction was considered for the generation of the scattered wave. This holds true, in the case of two continuously sent incident waves in steady state. However, the before mentioned use of phased arrays with a pulse generator creating incident waves at programmable angles, results in pulsed incident waves with a certain amount of cycles. To the best knowledge of the author, currently available hardware for the control of phased arrays only uses pulse generators for the creation of incident waves, as they are mainly developed for linear techniques. In order to improve this nonlinear technique, hardware for the control of phased array antennae using wave generators with a circuit to precisely control the phase shift (Phased locked loop PLL) between the signals on multiple channels could be developed. The incident waves generated by this pulse generator hardware are tone bursts, which limits the spatial length of the incident waves and leads to a change of the interaction volume over time. Chen *et al.* analyzed this phenomenon in [18] for 1D collinear wave mixing.

The second aspect, is the considered width of the wave pulse characterized by the width over which a plane wave front can be assumed. This is modeled by the physical boundaries of the phased array, i.e., the right and left most transducer elements. Dependent on the current steering angle the geometric width of this assumed plane wave front changes. Similar modeling for the interaction volume was done by Zhang *et al.* in [25]. Additionally, the validity of this assumption is supported by the fact that the generation of a resonant wave is sensitive to the exact matching of the resonance condition (angle between the plane wave fronts). This is also used in [24], where relaxation of the condition is used to reduce the contribution from the nonlinearity of the surrounding media for the inspection of an imperfect interface.

These assumptions lead to the modeling of the wave pulses emitted by the two phased

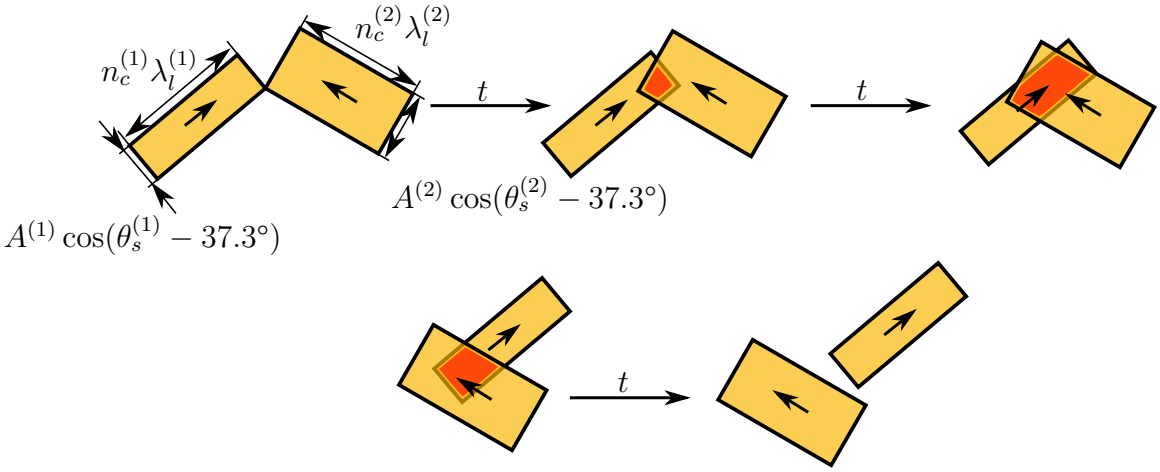

Figure 3.8: Illustration of beams in yellow with spatial length calculated as number of cycles $n_c^{(1)}$ times wavelength $\lambda_l^{(i)}$ and width calculated as aperture $A^{(i)}$ times cosine of steering angle shifted by wedge angle $\cos(\theta_s^{(i)} - 37.3°)$. Mixing volume V in red as the overlap of pulses changes over time.

arrays as two rectangles, with length according the spatial length of the pulses

$$\text{length} = n_c^{(i)}\lambda_l^{(i)} \tag{3.15}$$

and width according to the projected aperture

$$\text{width} = A^{(i)}\cos(\theta_s^{(i)} - 37.3°), \quad i = 1, 2 \tag{3.16}$$

of the beam at the used steering angles. Here $A^{(i)}$ are the physical apertures determined by the distance between the left and right most transducer of an array, $n_c^{(i)}$ are the number of cycles, $\theta_s^{(i)}$ are the steering angles and $37.3° = 90° - 52.7°$ is the at the beginning of this chapter mentioned offset from the wedges (measured from the horizontal). In Figure 3.8 a schematic depiction of two mixing pulses at different instants in time is shown. The effective mixing volume for a time t is determined as the overlap region of the two rectangles representing the pulses. This results in the modulation of the resonant wave amplitude by a function $V(t)$. For example, in figure 3.9, the change of the mixing volume V over time and the modulated resonant wave for the mixing point $x_m = 0.3, y_m = 0.25$ is shown.

Figure 3.9 was achieved by numerical computation of the overlap region in contrast to the analytical integration done in [18] for the 1D case, because no closed analytical expression can be found for an arbitrary polygon changing over time.

3.4 Nonlinearity and crack modeling

The contribution of micro-cracks, dislocations and other damage or imperfections in the material micro-structure to the nonlinear response of a material is studied in different recent publications. Overall, a proportionality of the quadratic nonlinear response on the crack density was found by different authors [9, 10, 31, 32]. An overview of related work was given in section 2.4. However, it is difficult to develop an analytical model which is capable of describing the physical phenomena resulting in an increase of quadratic elastic nonlinearity. V. E. Nazarov and A. M. Sutin [33] derived a model considering a solid with randomly oriented cracks. In their model the effect of nonlinearity is incorporated by the additional displacement resulting from the cracks when normal stress is applied. This overall additional change in volume caused by the cracks is modeled by a Taylor series approximation which coefficients are derived from physical forces inside the crack when different types of asperities are compressed against each other. A different approach was formulated by C. Pecorari [31]. Instead of partially closed cracks, which faces are not in full contact with each other, he also considered clapping of cracks meaning the full closure of conforming crack faces resulting in a directional change of the normal component of the traction vector at the crack. In his work, the change in the elastic properties caused by this effect is modeled by a perturbation term contributing to the stiffness matrix in the constitutive relationship.

In practical applications however, the acoustic nonlinearity parameter β is used as a measure for the nonlinearity of the measured region. There are different types of acoustic nonlinearity parameters in the literature. Considering the wave equation for 1D wave propagation of longitudinal and transverse waves, the elastic parameters on the right-hand side

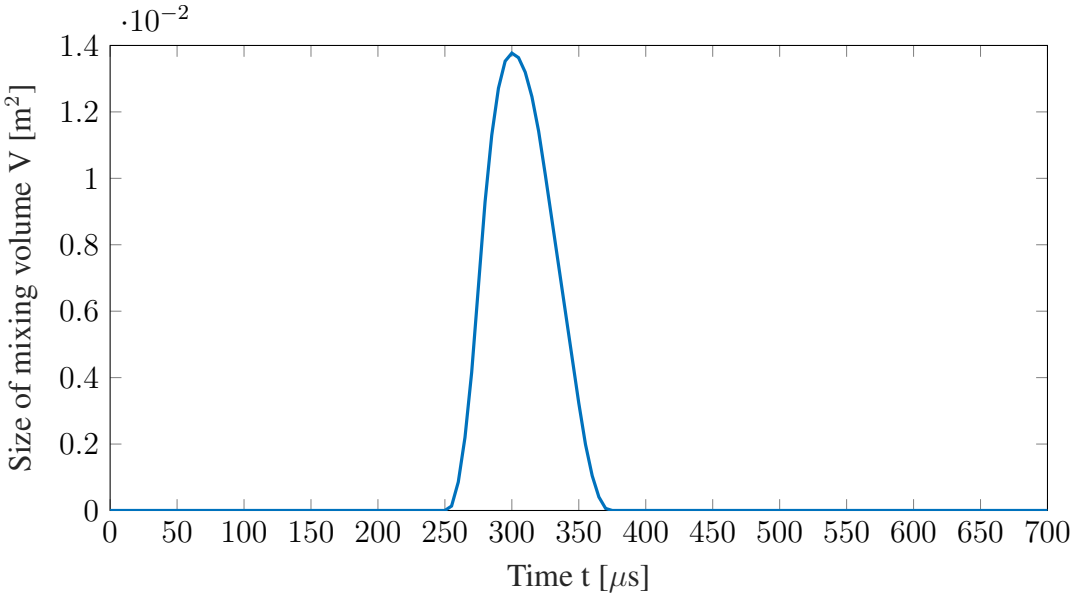

(a) Size of interaction area of pulses over time after first pulse is fired.

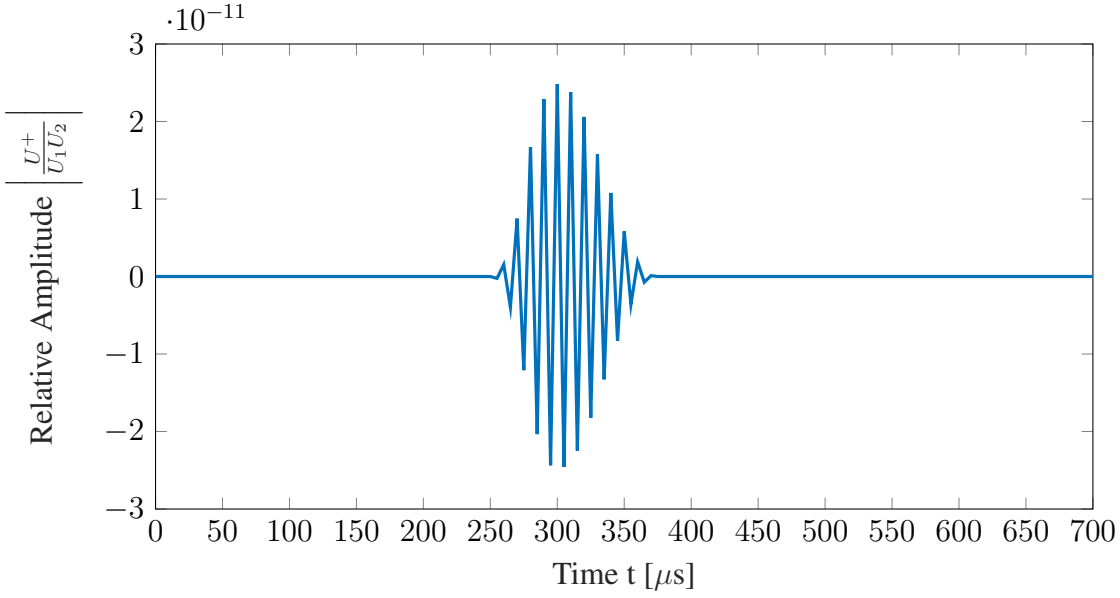

(b) Simulated resonant wave for mixing point $x_m = 0.3\text{m}, y_m = 0.25\text{m}$.

Figure 3.9: Interaction volume changes over time (a) as overlap region of pulses change, thereby amplitude of resonant wave (b) is modulated for mixing point $x_m = 0.3\text{m}, y_m = 0.25\text{m}$.

can be condensed as

$$\beta_L = 3 + 2\frac{l+2m}{\lambda+2\mu}, \quad \beta_T = \frac{\lambda+2\mu}{\mu} + \frac{m}{\mu}, \tag{3.17}$$

called the longitudinal and transverse acoustic nonlinearity parameters respectively [9, 18]. Because the measured parameter in experiments is the voltage of the transducer receiving the resonance wave, which is proportional to its amplitude, the relative acoustic nonlinearity parameter

$$\beta_{rel} = \left| \frac{U^{\pm}}{U^{(1)}U^{(2)}} \right| \tag{3.18}$$

is used as a relative measure of nonlinearity and will also be used in this thesis. An exact measure would require the exact knowledge of all absolute quantities in equations (3.9) and (3.12). In contrast to, the case of collinear wave mixing, where parameters β_L and β_T can be used and the mixing condition always stays the same, non-collinear shear wave mixing only provides $\beta = \beta(a)$ as a function of the current mixing condition for constant elasticity parameters. This means, that even two mixing points with the same nonlinearity will give different resonance wave amplitudes. This issue will be further discussed in sections 4.2 and 4.4.

CHAPTER 4
RESULTS

In this chapter, the main results of this thesis, comprised of an analysis of the measurement technique specifications and limitations, are presented. Section 4.1 is concerned with the effects resulting from the design of the phased arrays. Limiting factors for the steering angle and the degradation of the beam profile for large angles is discussed. In Section 4.2, the sensitivity of the proposed technique dependent on the mixing point for both types of polarization is analyzed. In Section 4.3, the relative attenuation dependent on the wave paths for a certain mixing point is calculated. Finally, in Section 4.4 simulative results for a concrete block with an aggregation of micro-cracks are shown and the compensation of unknown TOE in the intact case is discussed.

4.1 Beam steering and phased array design analysis

Beam steering is the basic functionality needed when using phased arrays for wave mixing, because this controls the angle of the generated incident waves and thereby the achieved mixing angle $\Delta\theta$ and the mixing point for fixed array positions. Design parameters of the phased array, e.g., element spacing, element width and number of elements, influence the beam profile and thereby the maximum feasible steering angle. An extensive study of phased array design for beam steering via beam profile modeling simulation can be found in [34] and an optimization of directivity and steerability was done in [35]. In the following, figures are made for concrete when basic relationships between design parameters and limiting factors are demonstrated, because results are similar for other cement based materials and concrete is the most limiting one. However, results for all materials from table 3.1 are shown for the maximum feasible steering angle.

Under the assumption that the element width δ_e is much smaller than the wavelength

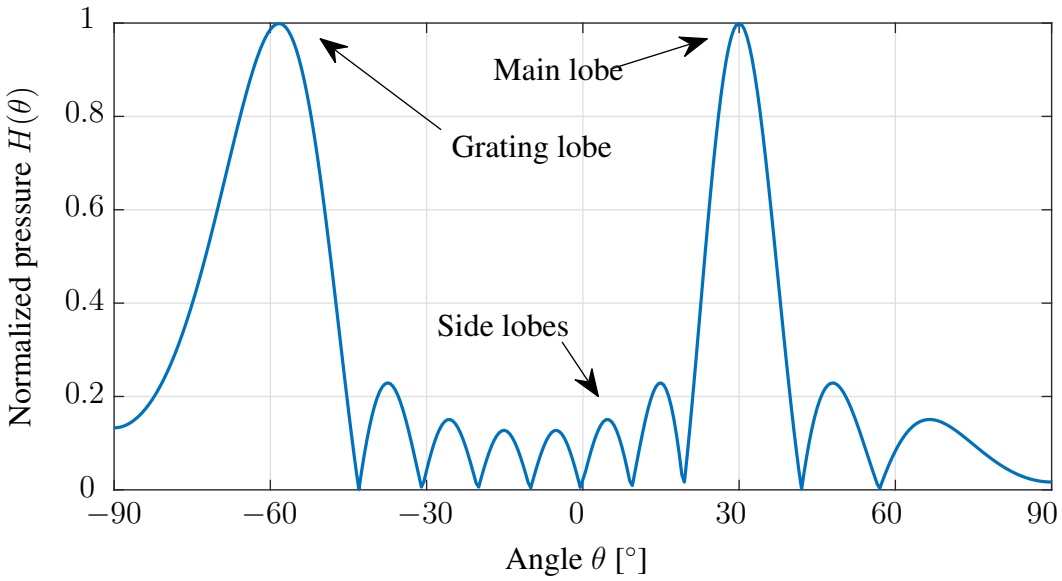

Figure 4.1: Pressure normalized by pressure in steering direction $H(\theta)$, with $\theta_s = 30°$, $f = 80\text{kHz}$, $c_T = 2702\text{m}\,\text{s}^{-1}$ (concrete), $\lambda_l = 0.0338\text{m}$, $N = 8$ and $\delta_x = 0.025\text{m}$.

λ_l ($\delta_e/\lambda_l \ll 1$), the beam profile can be modeled as the superposition of point sources according to Huygens principle. From [35] the pressure in the direction θ normalized by the pressure in the steering direction θ_s for a linear array can then be modeled as

$$H(\theta) = \left|\frac{p(r,\theta,t)}{p(r,\theta_s,t)}\right| = \left|\frac{\sin(\pi\delta_x N(\sin\theta_s - sin\theta)/\lambda_l)}{N\sin(\pi\delta_x(\sin\theta_s - \sin\theta)/\lambda_l)}\right|. \tag{4.1}$$

Modeling for three dimensional beam steering with a matrix array can be found in [36], but will not be further considered in this work. In this thesis, design parameters $N = 8$ and $\delta_x = 0.025\text{m}$ for in plane steering with the phased array shown in figure 3.5 are used, which is an example for the currently available hardware on the market. A simulation of the normalized pressure profile in concrete for beam steering can be seen in figure 4.1. Three different types of lobes can appear, the desired main lobe in the steering direction, side lobes and under certain conditions grating lobes. Grating lobes appear, if the inter-element spacing is $\delta_x > \lambda_l/2$, which can be seen as spatial aliasing following from the Nyquist sampling theorem. For $\delta_x = 0.025\text{m}$ in concrete ($c_T = 2702\text{m}\,\text{s}^{-1}$) grating lobes

appear for wavelengths smaller than $0.05\mathrm{m}$ or frequencies higher than $\sim 54\mathrm{kHz}$. In non destructive evaluation (NDE) with linear ultrasonic techniques, the appearance of grating lobes is a limiting factor for the steering angle, because it causes a pressure in an undesired direction with the same amplitude as in the steering direction, which is deleterious for the measurement signal quality. Therefore, in linear applications phased arrays are designed to prevent grating lobes for the used nominal frequency. This is done by choosing a compromise between selecting the element spacing small enough to prevent grating lobes for a certain steering angle range, suiting the respective wavelength in the material inspected for a specific application (e.g. weld inspections), but keeping it large enough to maintain directivity (in the extreme case $\delta_x \to 0$ collapsed to a point source with no directivity). However, for the application of nonlinear wave mixing techniques the frequency has to be changed matching the mixing condition equation (3.3), which makes it hard to find a design preventing grating lobes for a range of frequencies. But for wave mixing only the sector from $0°$ to $90°$ is relevant, in which grating lobes can be avoided. In Addition, the signal to be measured for wave mixing has the sum frequency of the incidence wave, which makes it possible to filter out any disturbing signals of other frequencies like the side wall reflected grating lobe beams (frequency discrimination). Furthermore, the resulting resonant wave vector is the sum of the incident wave vectors resulting in a fairly different propagation path than the grating lobe waves (spatial discrimination). The more crucial limiting factor for the maximum steering angle in the considered measurement technique is the loss of directivity as the beam width increases with the steering angle. An example of the increasing beam width up to coalescence of the beam with the side wall is shown in figure 4.2. The main lobe width, normalized by π to get values between 0 and 1, is calculated in [35] as

$$q = \frac{1}{\pi}\left[\sin^{-1}\left(\sin\theta_s + \frac{\lambda_l}{N\delta_x}\right) - \sin^{-1}\left(\sin\theta_s - \frac{\lambda_l}{N\delta_x}\right)\right], \tag{4.2}$$

here small values correspond to good directivity. The normalization is chosen such that a

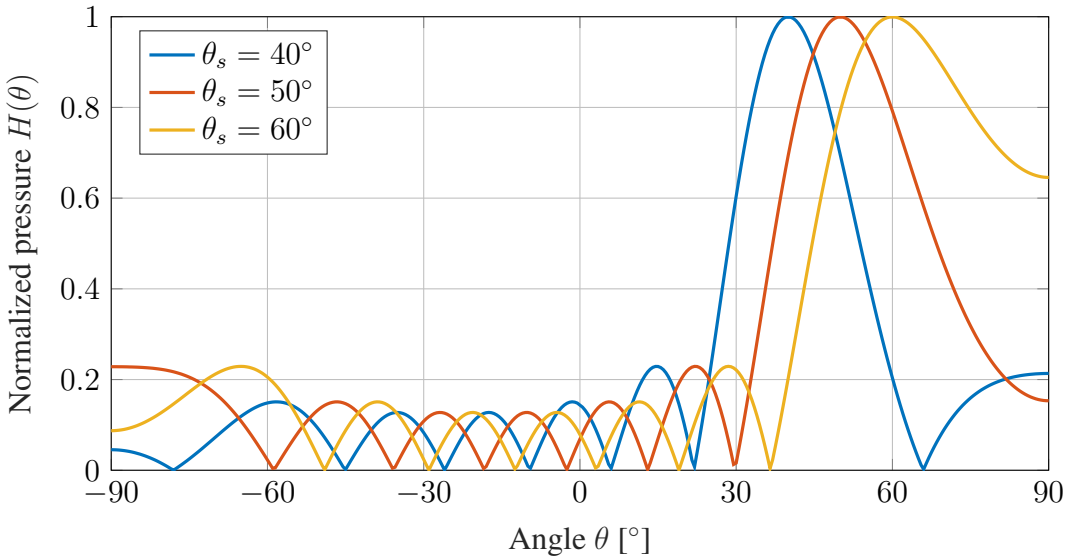

Figure 4.2: Pressure normalized by pressure in steering direction $H(\theta)$ for $\theta_s = 40°$, $50°$ and $60°$, with $f = 50\text{kHz}$, $c_T = 2702\text{m}\,\text{s}^{-1}$ (concrete), $\lambda_l = 0.054\text{m}$, $N = 8$ and $\delta_x = 0.025\text{m}$.

width of 1 corresponds to $180°$ and smaller values of q can be interpreted as the degree percentile of the infinite half-space occupied by the beam width. In Figure 4.3, the normalized lobe width q is shown for different steering angles θ_s and frequencies f. One can observe, that the slope of the lobe width q increases at the end for all frequencies, when the right side of the main lobe merges with the side wall. A condition for the maximum feasible steering angle can then be formulated as the angle when the zero pressure to the right-hand side of the main lobe reaches $90°$ at

$$\theta_{smax} = \sin^{-1}\left(1 - \frac{\lambda_l}{N\delta_x}\right). \tag{4.3}$$

This maximum feasible steering angle for different frequencies and materials is shown in figure 4.4. All materials have an increase in the maximum feasible steering for higher frequencies, with concrete and cement paste being close to each other and higher possible steering angles in mortar at all frequencies due to its lower shear wave velocity. A good compromise for beam directivity while maintaining a broad frequency range for wave mix-

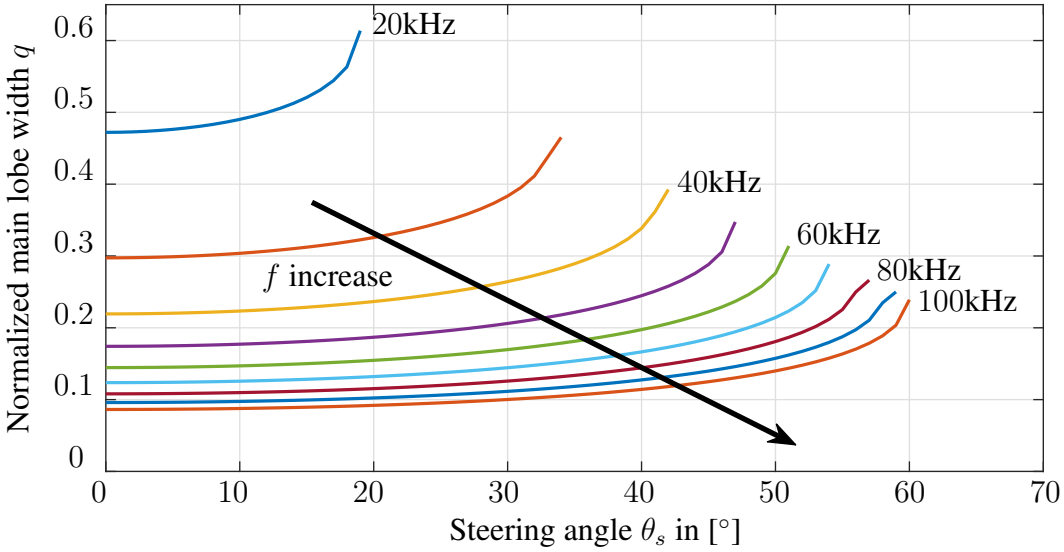

Figure 4.3: Normalized main lobe width q for frequencies 20kHz to 100kHz, with $c_T = 2702\mathrm{m\,s^{-1}}$ (concrete), $N = 8$ and $\delta_x = 0.025\mathrm{m}$.

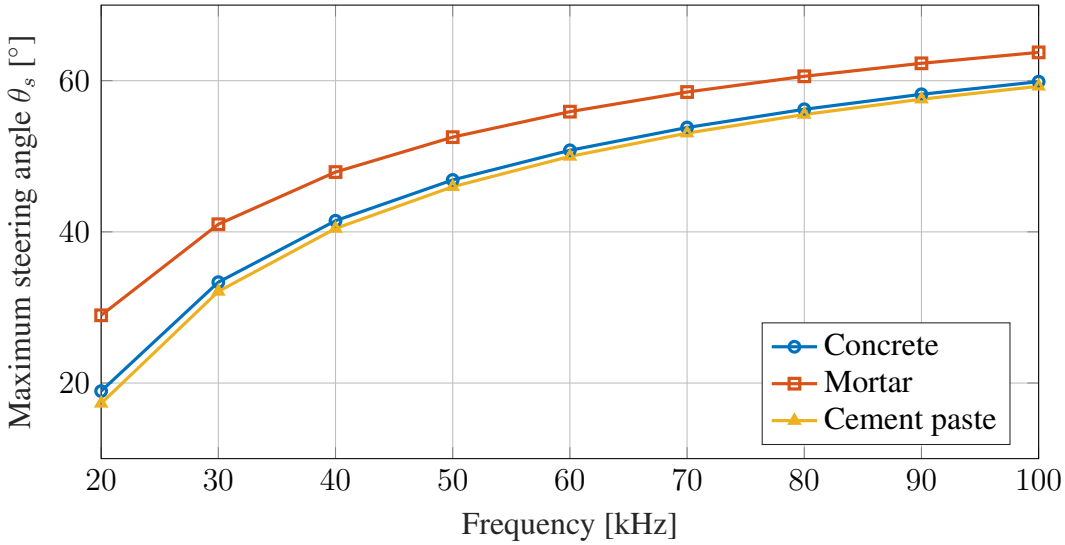

Figure 4.4: Maximum steering angle θ_{smax} for a single array at frequencies 20kHz to 100kHz, with $c_T = 2702\mathrm{m\,s^{-1}}$ (concrete), $c_T = 2063\mathrm{m\,s^{-1}}$ (mortar), $c_T = 2810\mathrm{m\,s^{-1}}$ (cement paste), $N = 8$ and $\delta_x = 0.025\mathrm{m}$.

ing in all materials, is to use only frequencies in the range 30kHz to 100kHz resulting in a beam width range of approximately 0.09 to 0.4 and a maximum steering angle greater than $34°$ for the used frequencies for all materials. However, it is desirable to choose the lowest possible frequencies for better signal strength, as lower frequencies get less attenuated. But it is inherent to figure 4.3, that lower frequencies lead to larger beam widths at all steering angles. Therefore, it is advisable to set the array with the smaller steering angle for the desired mixing point to the lowest possible frequency of 30kHz, while setting the other array with the larger steering angle to the higher frequency $a \times 30\text{kHz}$ according to the frequency ratio a resulting from the mixing condition. Thus, a good size of the feasible scanning region is obtained, while minimizing the path attenuation.

Another conclusion of this analysis is the in section 3.1 proposed design with the phased arrays on wedges. Thus, creating an angle offset for the beams, in order to minimize the needed steering angles for the region of interest. Here the material of the wedges should be selected to match the impedance of the concrete material to get the best possible transmission coefficient at the interface. Ideal would be to use the same material for the wedges and specimen with perfect coupling and no interface, thus only producing an angle offset and no refraction. Otherwise the use of materials with low wave velocities, e.g., Teflon is recommended, leading to smaller incidence angles needed at the interface to keep the transmission coefficient high and the reflection coefficient low to minimize losses. Using Equation (4.1), the superposed pressure field of the beams emitted by the two arrays can be visualized. Figure 4.5 shows the two beams and in red the boundaries of the plane wave fronts resulting from the assumption in section 3.3 for wave mixing with and without wedges in the setup. Without wedges the larger steering angle of the left array leads to a degradation of the beam, spreading the energy over the whole green sector. Whereas in the setup with wedges the beam clearly stays in the projected boundaries until the mixing volume is reached and the pressure is concentrated at the mixing point. In the case without wedges the red boundary corridors are smaller as the projected apertures are smaller,

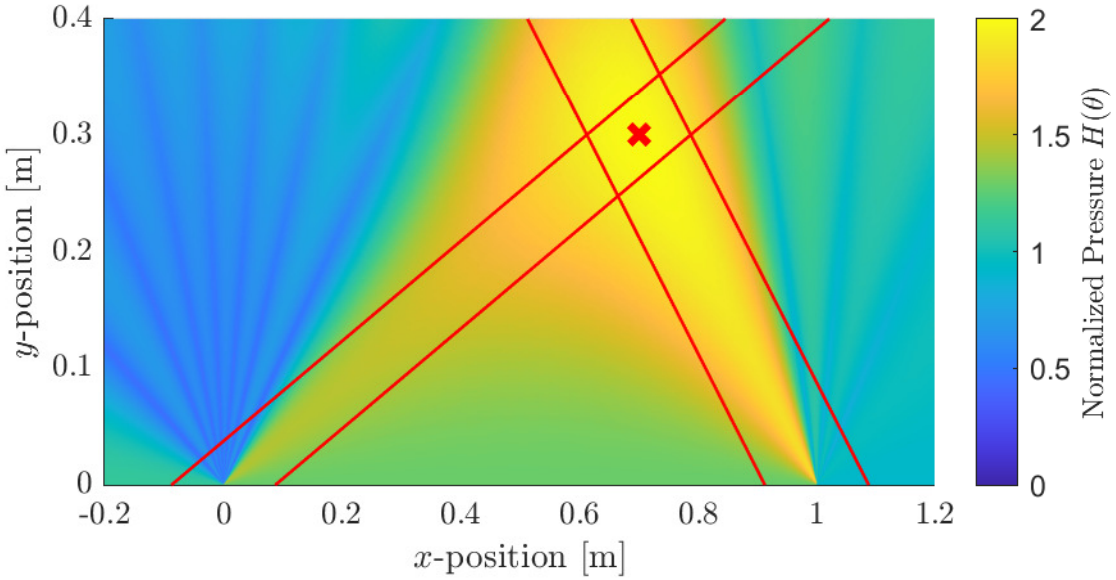

(a) Beam profiles for mixing without wedges.

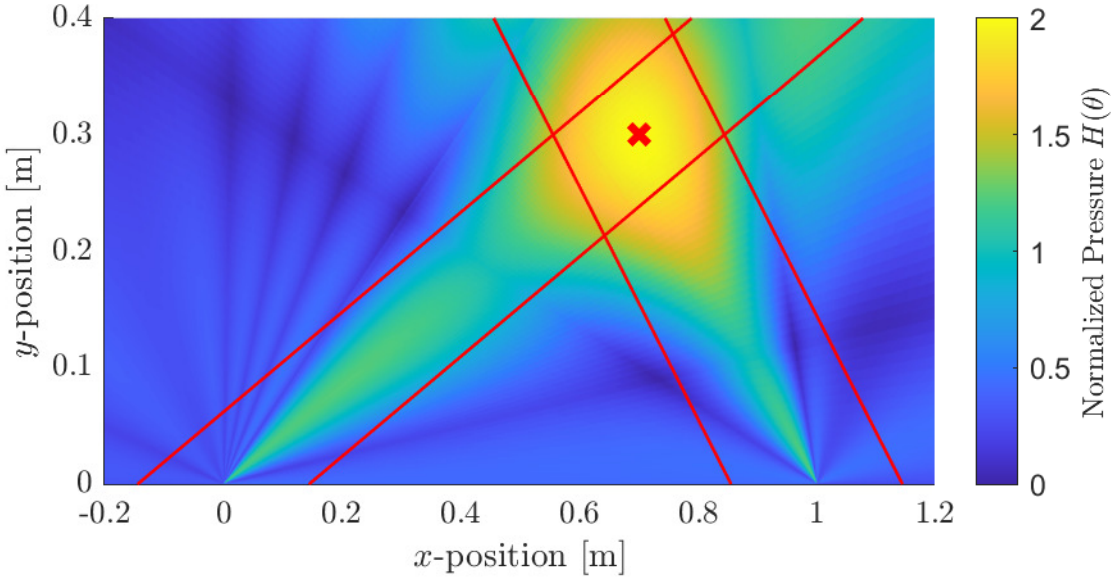

(b) Beam profiles for mixing with wedges.

Figure 4.5: Normalized pressure field for two superposed beams (left beam 53kHz, right beam 30kHz, $a = 1.7685$) crossing at mixing point $x_m = 0.7, y_m = 0.3$ shown as red marker. Geometric boundaries for plane wave fronts through projection of physical apertures shown as red lines.

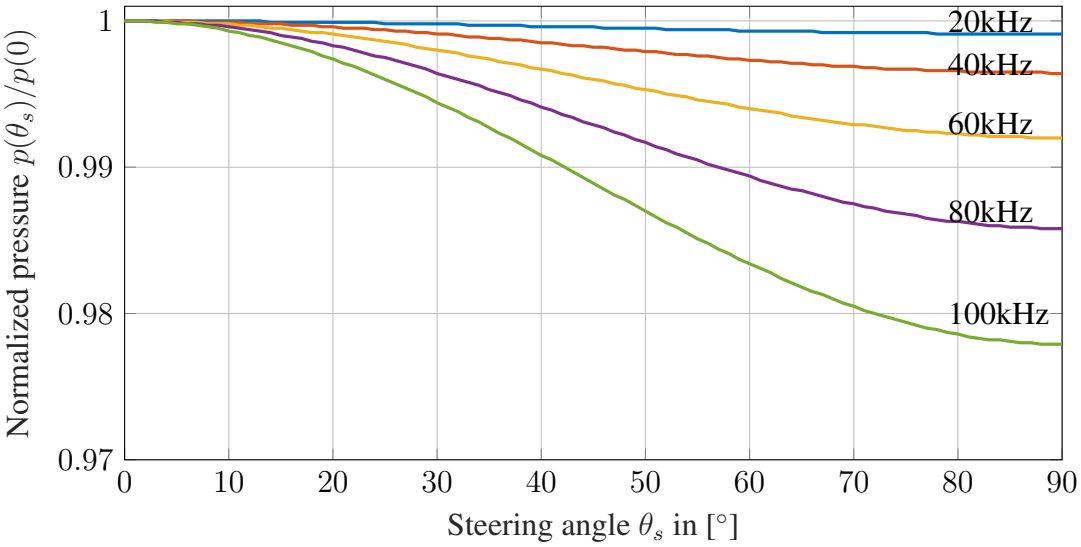

Figure 4.6: Pressure in steering direction normalized by pressure amplitude at $\theta_s = 0°$ for frequencies from 20kHz to 100kHz, with $\delta_e = 1e - 3\text{m}$.

due to the larger angle between the vertical to the array surface and the steering direction. This does not account for the characteristic of the waves being pulses limited in time, but it shows that the overlap region is a good approximation for the maximum interaction volume and the rays outside of the red boundaries are further diverging not contributing substantially to the generation of the resonant wave. A more accurate determination of the interaction volume would require a (computationally heavy) dynamic FEM analysis which is out of the scope of this thesis.

Another aspect to consider is the pressure in the steering direction compared to pressure of a beam at $0°$. This pressure is calculated as

$$p(\theta_s) = \text{sinc}(\pi \delta_e \sin\theta_s / \lambda_l). \tag{4.4}$$

In Figure 4.6, the pressure dependent on the steering direction in concrete for different frequencies is shown. As this pressure decreases at most by 2.2% the influence of the steering angle can be neglected for the amplitude calculation in equations (3.9) and (3.12). However the width over which the amplitude is distributed is considered through the size

of the interaction volume modeled in section 3.3.

4.2 Sensitivity analysis

As mentioned in section 3.1, the resonant wave amplitude is dependent on the current mixing condition, meaning the the mixing angle to scan a certain point for a fixed geometry and the respective frequency ratio from equation (3.2). The resulting resonant wave amplitude is also different for different types of polarization, which was shown in figure 3.4. Furthermore, it depends on the mixing volume modeled in section 3.3, which is determined by the geometry of the setup. And in the previous section, it was discussed that better directivity is achieved, if the beam with the smaller steering angle is set to the lower frequency. Taking all these results into accout, figure 4.7 shows the normalized nonlinearity parameter β_{rel} for every point inside a specimen, assuming TOE's for concrete from table 3.1 in the intact state, for both polarization cases respectively. One can see in figure 4.7a, that with out of plane polarized shear incident waves higher sensitivity is achieved in the central region. Whereas in figure 4.7b, the in plane polarized shear waves lead to higher sensitivity in the top and bottom region.

These results have to be considered in combination with attenuation inside the material. As higher frequencies get attenuated more, it is better to have a shorter path for the resonant wave which has the sum frequency of the incident waves. Furthermore, low frequency ratio values a are preferred, to also keep both incident wave frequencies low. This means, that the region close to the receiver side of the material is subject to less attenuation, which will be discussed in the next section. Overall, in this scenario the in plane polarization of shear waves might be preferred in highly attenuative cement based materials. However, both polarizations can be considered for less attenuative materials, e.g., for metal material inspections.

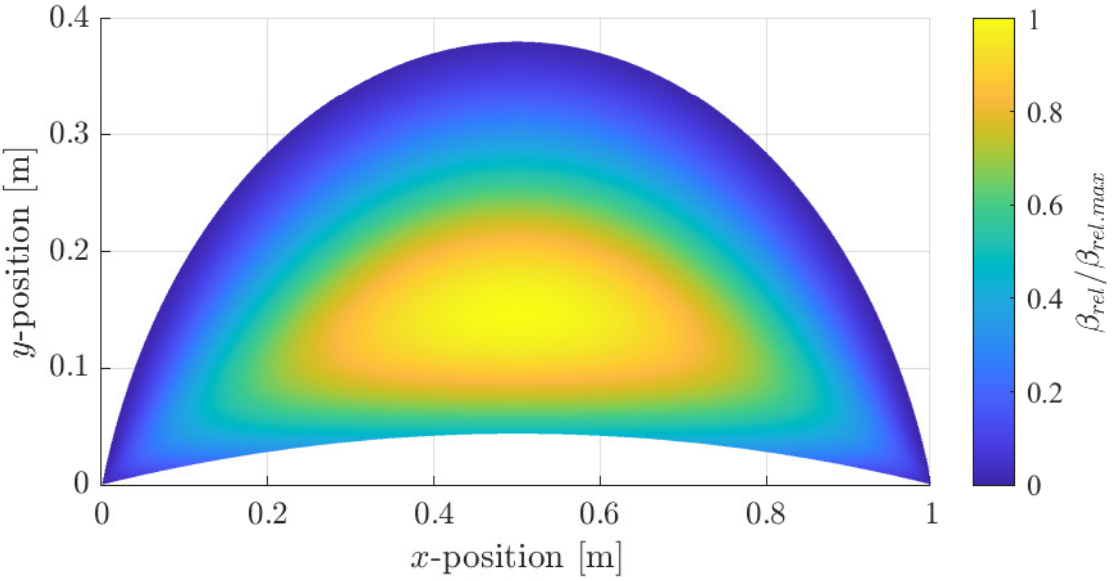

(a) Out of plane polarization.

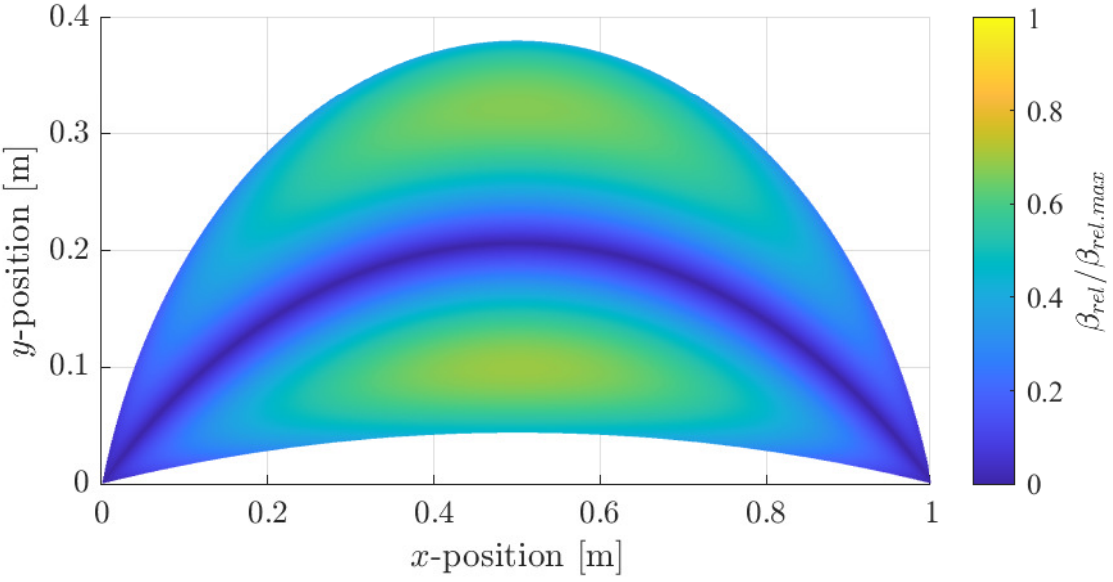

(b) In plane polarization.

Figure 4.7: Normalized parameter β_{rel} for different polarization with two shear incident waves, dependent on the position in the scanning zone inside $0.4\mathrm{m}$ thick concrete. With $1\mathrm{m}$ distance between arrays, incident wave with smaller steering angle at $30\mathrm{kHz}$ and other incident wave at $a \times 30\mathrm{kHz}$ according to the angle condition and interaction volume based on equal apertures. Material properties from concrete in table 3.1.

4.3 Path attenuation for non-collinear wave mixing

For the presented measurement technique it is of particular interest to determine the expected attenuation in the region of interest in addition to the sensitivity. Thus, assessing the region for which good measurement results can be expected. The two main mechanisms of attenuation are geometric and material attenuation. Geometric attenuation considers the decrease in amplitude as the cylindrical or spherical wave front spreads in the specimen. Material attenuation considers absorption of the energy by the material converting kinetic to thermal energy (intrinsic) and scattering effects at heterogeneous particles inside the material (extrinsic). In practice, extrinsic and intrinsic material attenuation are hard to distinguish and only the overall attenuation by the material is described by one attenuation parameter α_{0L} for longitudinal and $\alpha_{0T} \approx \alpha_{0L}/c$ for transverse waves. In general, the wave amplitude subject to attenuation can be written as

$$\begin{aligned} A(r,f) &= \frac{A_0}{r^{\eta_g}} e^{\alpha(f) r}, \\ \alpha(f) &\approx \alpha_0 f^{\eta_m} \end{aligned} \tag{4.5}$$

with initial amplitude A_0, propagation distance r, frequency f, material attenuation coefficient α_0 and exponential material and geometric parameters η_m and η_g. For spherical wave fronts in a volume, the geometric attenuation exponent is $\eta_g = 1$. Cylindrical wavefronts, e.g., Rayleigh surface waves would have an η_g of 0.5. The material exponent parameter η_m for rock, sediment and concrete is approximately 1. For metals it would be $\eta_m = 2$ and most soft tissues have η_m in the range of 1 to 2. In [37] the attenuation for different compositions of cement based material was measured for a range of frequencies. Therein, one can see that a linear relationship between frequency and attenuation can be assumed for frequencies below $100kHz$.

As geometric attenuation is not specific to the material and may depend on the shape and sidewall reflections inside the specimen, it will not be considered in this analysis. Fur-

thermore, for heterogeneous media the composition plays an important role for the properties of the material. Concrete for example, is made of water, sand, aggregates and cement. Therefore, its properties are strongly dependent on the mixing ratios of these components, especially water to cement (w/c) and aggregate to cement (a/c) ratio, which is investigated in [37]. Additionally, the size of the aggregates has an influence on the attenuation inside the material. Aggregates influence the attenuation not only intrinsic through their amount of material absorption, but also extrinsic as their size and concentration influences the amount of scattering. Therefore, the focus here is on the frequency and wave path dependent relative attenuation without considering a particular material, to find out how the attenuation depends on the position of the arrays and the chosen scanning point.

During non-collinear shear wave mixing, there are three paths along which waves get attenuated. The paths of the two shear incident waves and the path of the longitudinal resonant wave. Dependent on the point to be scanned, the three propagation distances as well as the frequencies to fulfill the mixing condition equation (3.4) vary. Using the following proportionalities and relations for the unattenuated and attenuated wave amplitudes

$$\begin{aligned} U_{att}^{(1)} &= \exp(-\alpha_{0T} r_1 f_1) U^{(1)}, \quad U_{att}^{(2)} = \exp(-\alpha_{0T} r_2 f_2) U^{(2)}, \\ U_{att}^{+} &= \exp(-\alpha_{0L} r (f_1 + f_2)) U_0^{+}, \quad U_0^{+} \propto U_{att}^{(1)} U_{att}^{(2)}, \\ \Rightarrow U_{att}^{+} &\propto \exp(-\alpha_{0L}(r(f_1 + f_2) + r_1 f_1/c + r_2 f_2/c)) U^{(1)} U^{(2)}, \end{aligned} \tag{4.6}$$

with a typical conversion to dB

$$20 \log_{10}(U_{att}^{+}) \propto -\alpha_{0L}(r(f_1 + f_2) + r_1 f_1/c + r_2 f_2/c) 20 \log_{10}(e) + 20 \log_{10}(U^{(1)} U^{(2)}), \tag{4.7}$$

a relative measure for the path attenuation by substracting offset and factoring out constants

is defined as

$$Att_{rel} := (r(f_1 + f_2) + r_1 f_1/c + r_2 f_2/c). \tag{4.8}$$

Here r_1, r_2, r and f_1, f_2, f_1+f_2 are path lengths and frequencies of the incident and resonant waves respectively. Furthermore, the subscript att denotes attenuated amplitudes and U_0^+ denotes the resonant wave amplitude generated by the attenuated incident waves at the mixing volume. Note that the left out factor $-\alpha_{0L} 20 \log_{10}(e)$ is just a conversion of the material attenuation from Np to dB and the offset is just dependent on the incident wave amplitudes, thus equation (4.8) gives a material and incident amplitude independent relative measure for the attenuation of every scanning point.

According to section 4.1, it is favorable to set the array with the smaller steering angle to a frequency of $30\mathrm{kHz}$ while the other array with the larger steering angle is set to a frequency of $a \times 30\mathrm{kHz}$. Note that the array with the smaller steering angle is also the array with the shorter incident wave path for the considered scanning region. For the different cement based materials from table 3.1 the velocity ratio c is in the range of 0.5 to 0.6, therefore equation (4.8) is evaluated for the average $c = 0.55$, as the results qualitatively look similar for this range of c values.

Figure 4.8 shows the path attenuation from equation (4.8) for all points in the scanning region, when a distance between the arrays of $1\mathrm{m}$ is selected. Mixing points closer to the opposite surface are subject to less attenuation. This is because the isogonic with mixing ratio $a = 1$ is closest to the opposite surface, so both incident waves can be set to the lowest frequency of $30\mathrm{kHz}$. Additionally, the resonant wave with the higher sum frequency of the two incident waves, has a shorter path through the medium for points closer to the opposite surface. Furthermore, mixing points with the same mixing ratio (c.f. isogonics in figure 3.3) have the same resonant wave frequency resulting in similar attenuation. However, mixing points closer to the bottom surface are subject to more attenuation. An idea

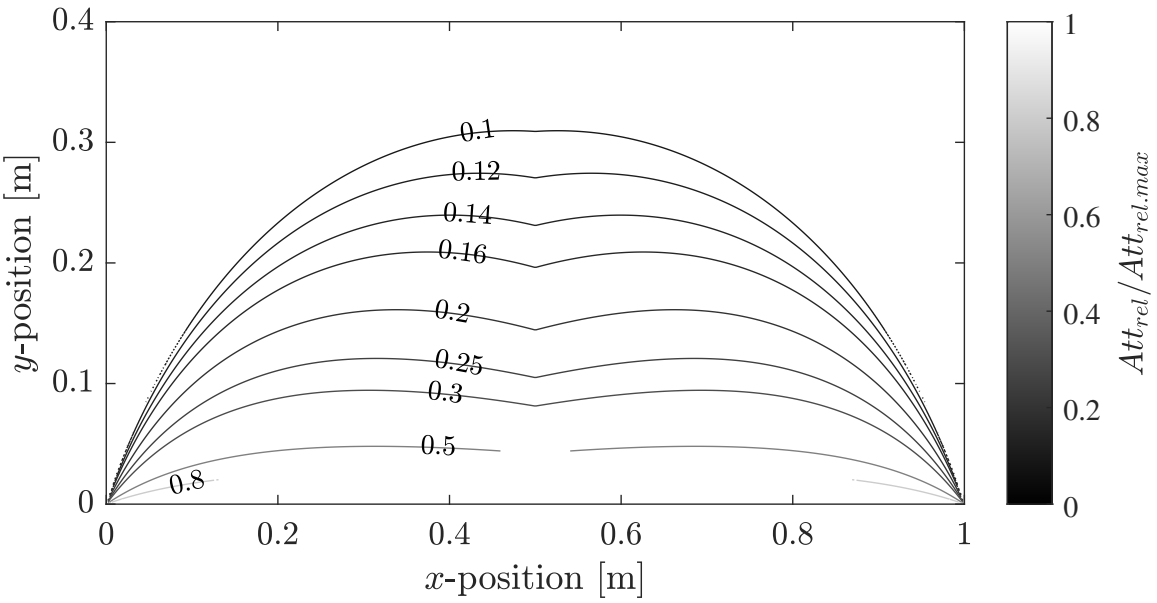

Figure 4.8: Normalized relative attenuation along wave paths for all points in scanning region, with resonant frequency $(1+a) \times 30\text{kHz}$, closer incidence wave frequency 30kHz, other incidence wave frequency $a \times 30\text{kHz}$, distance between arrays $L = 1\text{m}$ and $c = 0.55$.

would be to change the position of this scanning region by moving the arrays closer together. But this would result in a longer path for the resonant wave and the advantage of not having to move equipment around the specimen with this measurement technique is lost. However, attenuation is countered by the amplification of the resonance effect which increases with the size of the mixing volume. This results in a trade off between resolution and signal strength. An extreme example of this is the collinear mixing approach in steady state, where both incidence waves are propagating along the same line using the whole cross section for interaction. Thereby, a good signal strength is achieved, but no spatial distinction of the points in the cross section is possible.

4.4 Simulation of volume with micro-cracks

In this section, a measurement is simulated by modeling a crack volume through a relative increase of the TOE. The Murnaghan constants m, n or n are increased by 20% respectively in a circular region of radius 5cm around $x = 0.3\text{m}, y = 0.25\text{m}$. Attenuation, as discussed

in the previous section, is not considered here and can be compensated for by the respective path calculations for each scanning point. In Figure 4.9, the simulative result for an in plane and out plane measurement are shown. One can recognize a slight boundary of the circular shaped region, which is distorted to an oval due to the unequal axis scaling for better figure formatting. If all material parameters, including the TOE of an intact specimen, are known a priori, one can compensate for the sensitivity at different position and get the relative increase in $\beta_{comp.exact}$ shown in figure 4.10. Because the TOE are on a higher order of magnitude compared to the Lamé parameters, an increase of them by 20% also leads to an approximate increase of the relative acoustic nonlinearity parameter β_{rel} by 20%. However, in practice it is difficult to measure the TOE. In particular, an intact specimen of the same composition is needed for comparison. Therefore, an exact compensation for the sensitivity is often not possible. This problem arises from the fact that β_{rel} is a function of a, which changes for different mixing points when using non-collinear wave mixing. A collinear mixing technique, as presented in [38], does not have this dependency, but thereby no spatial discretization is possible, measuring an average of β_{rel} for every cross section. Furthermore, a collinear technique requires the movement of equipment to scan different cross sections slowing down the process of scanning a larger volume.

Nevertheless, an approximate compensation for the dependency on a can be achieved in post processing by using the a priori knowledge of $V, r, U_1, U_2, w_1, \lambda, \mu, \rho, c_L$ and c_T. For in plane polarization the compensation is

$$U^{+}_{comp} = U^{+}_{meas} \Big/ \left(\frac{U^{(1)} U^{(2)} \omega_1^3 V}{16\pi r \rho} \frac{1}{c_L^3 c_T^2} \right) - \Bigg[(\lambda + 2\mu) \left\{ (1 - c^2)(a + a^2) \right\} + (\lambda + 3\mu) \left\{ 2 \left((a + \frac{1}{a}) \frac{c^2 - 1}{2} + c^2 \right)^2 - 1 \right\} \Bigg] \tag{4.9}$$

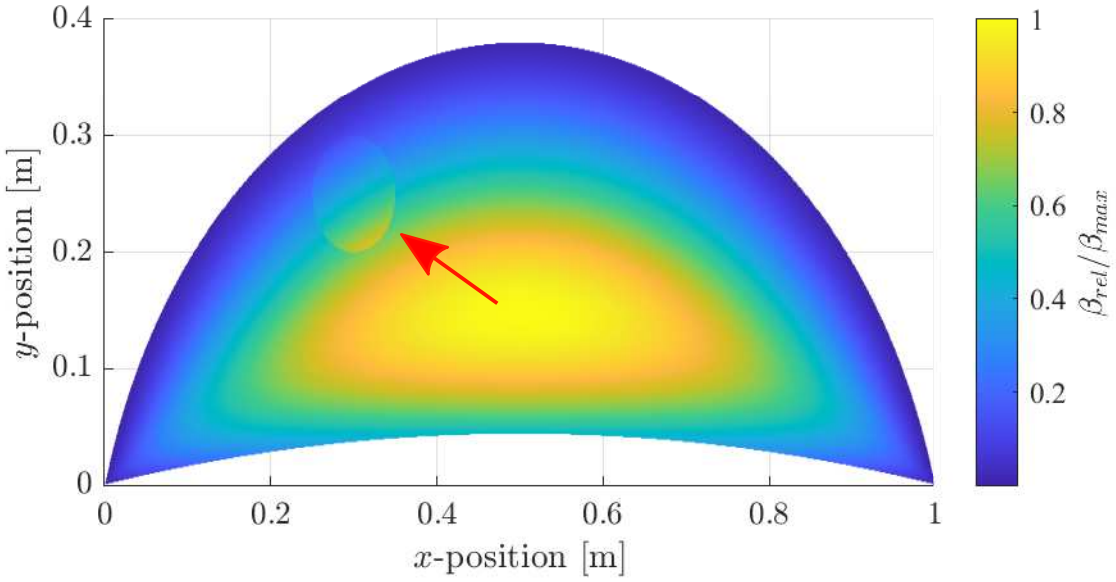

(a) Out of plane polarization.

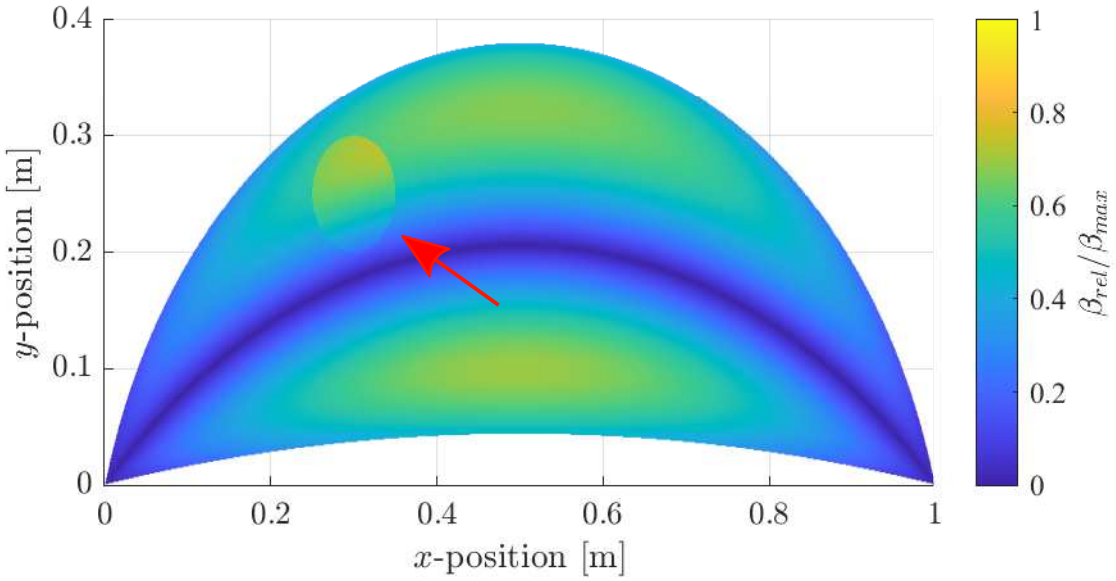

(b) In plane polarization.

Figure 4.9: Simulation of spherical volume with damage at $x = 0.3, y = 0.25$ with radius 5cm. TOE's are increased by 20% inside crack volume compared to specimen without damage.

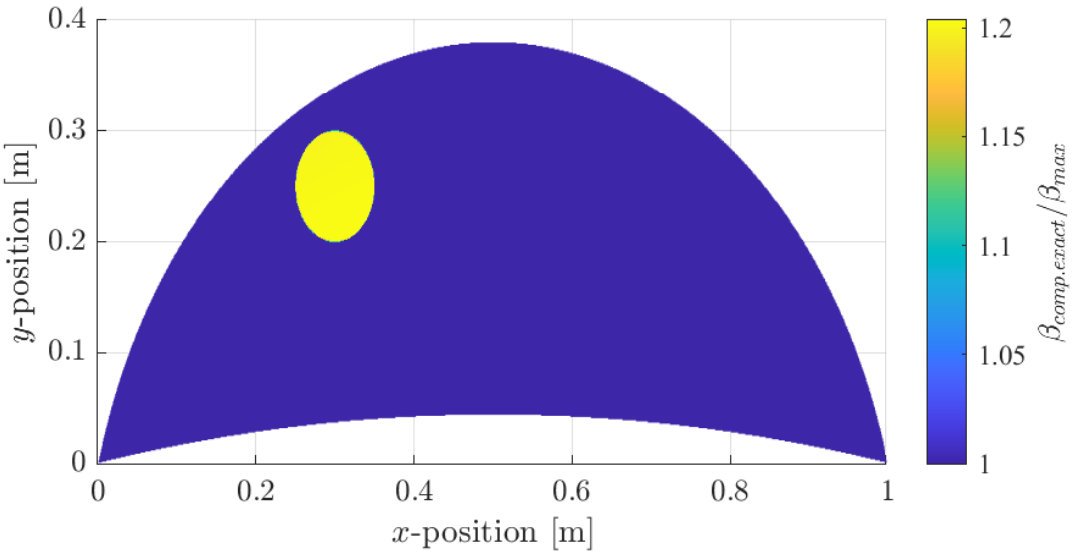

Figure 4.10: Simulation of spherical volume with damage at $x = 0.3, y = 0.25$ with radius 5cm. TOE's are increased by 20% inside crack volume compared to specimen without damage.

and for out plane polarization the compensation is

$$U^{+}_{comp} = U^{+}_{meas} / \left(\frac{U^{(1)} U^{(2)} \omega_1^3 V}{16\pi r \rho} \frac{1}{c_T^4 c_L} \right) - \left[\mu \left\{ (a^3+1)(c^2-1) + a(a+1)(c^2+1) \right\} + (\lambda+\mu) \left\{ c^2(3c^2-1)(a+a^2) + c^2(c^2-1)(a^3+1) \right\} \right]. \tag{4.10}$$

Here U^{+}_{meas} is the simulated measured and U^{+}_{comp} is the approximately compensated resonance amplitude. The approximately compensate acoustic nonlinearity parameter then is

$$\beta_{rel.comp.} = \frac{U^{+}_{comp}}{U^{(1)} U^{(2)}}. \tag{4.11}$$

In Figure 4.11, the approximately compensated results for in and out plane polarization are shown respectively. In the out of plane polarization case in figure 4.11a, a noticeable gradient is still visible, whereas in the in plane case in figure 4.11b only a slight gradient in the

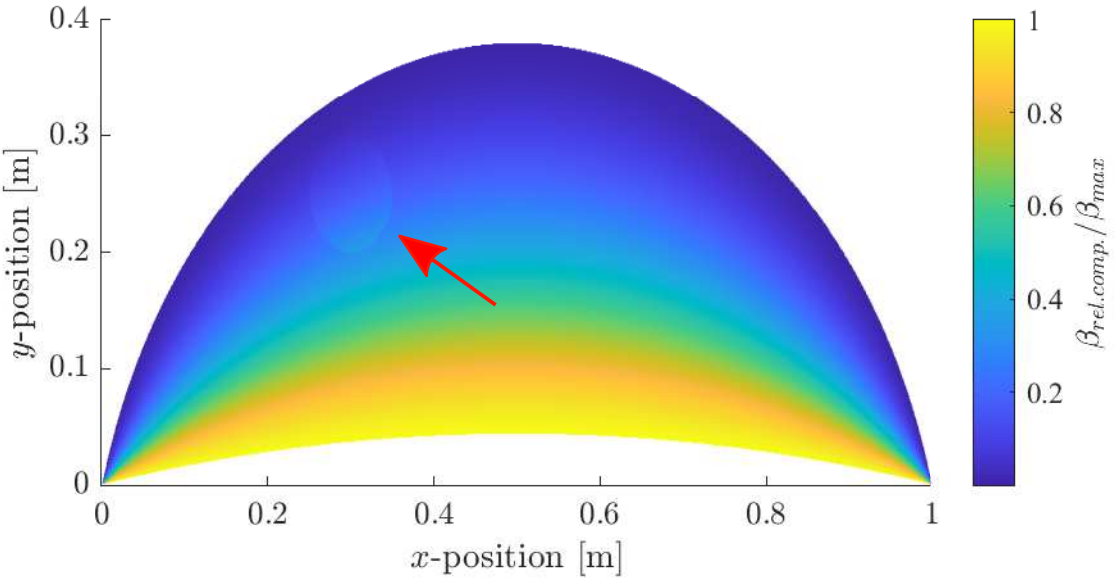

(a) Out of plane polarization.

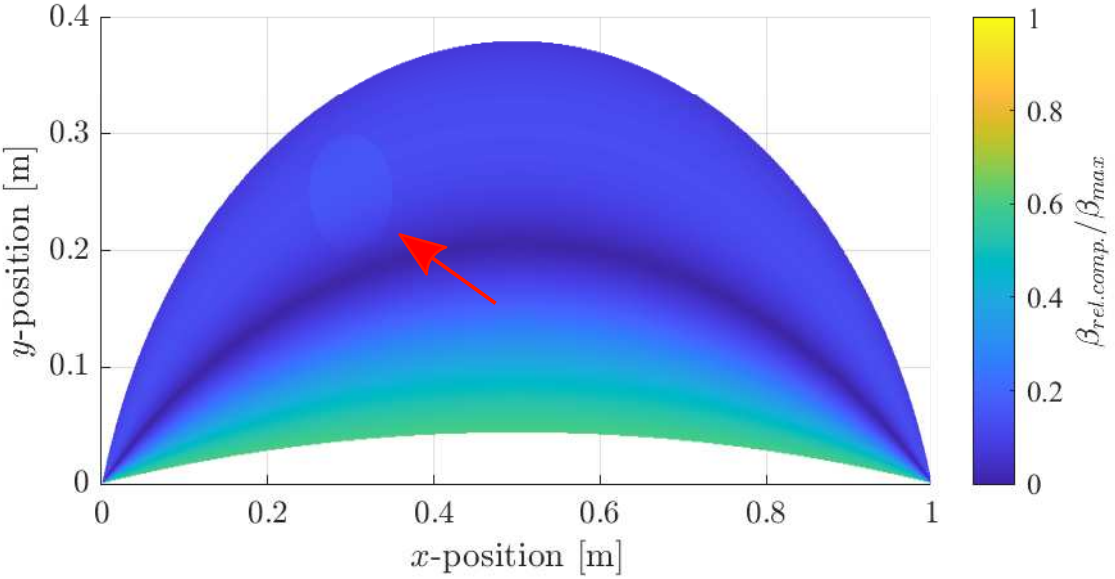

(b) In plane polarization.

Figure 4.11: Simulated nonlinearity parameter $\beta_{rel.comp.}$ approximately normalized using apriori knowledge of $V, r, U_1, U_2, w_1, \lambda, \mu, \rho, c_L$ and c_T.

bottom region and around the zero amplitude line is visible. This can be compensated for by measuring at multiple locations in an intact area to asses the background nonlinearity and calculate the relative increase in the measurement caused by micro-scale damage. For the in plane polarization only one Murnaghan constant m is unknown, therefore one measurement point would suffice to calculate compensation, whereas in the out of plane case m and n are unknown and at least two intact measurement points are needed. However, it is a good idea to get more measurement points and solve a least squares problem of the over-determined system of equations to account for measurement errors.

CHAPTER 5
CONCLUSION AND OUTLOOK

5.1 Conclusion

In this Thesis, a non-collinear shear wave mixing technique for the assessment of micro-scale damage in cement based materials was proposed and analyzed. Two phased arrays were used to generate the shear incident waves, giving the advantage of changing the beam angles without a physical change in the measurement setup.

In Chapter 2, the theoretical background in continuum mechanics in order to describe the nonlinear wave mixing phenomenon was given.

In Chapter 3, the necessary and sufficient conditions for the generation of a resonant wave in this setup were derived. From these conditions, scanning lines needing the same frequency ratio (isogonics) were calculated, with the $a = 1$ and $\Delta\theta = 105.4°$ isogonic building an upper bound of the scanning region for concrete. This line is a boundary dependent on the wave velocities, but its location can be changed by the distance L between the arrays, which can be adjusted dependent on the thickness of the specimen. Furthermore, the dependence of the resonant wave amplitude on the frequency ratio was shown for in and out of plane polarized shear waves. It was shown, that in plane polarization generates higher amplitudes for frequency ratios $a \leq 2.5$, whereas out of plane mixing generates higher amplitudes for frequency ratios $a > 2.5$. For phased arrays, the basic time delay laws for beam steering and beam focusing were discussed. Especially, beam steering is used as a key feature of phased arrays, in order to scan a specimen without physical movement of measurement equipment, besides the air coupled receiver on the other side of the specimen. As the amplitude of the resonant wave also depends on the size of the mixing volume, a model for the mixing volume was developed. Because of the use of wave pulses

instead of steady state continuous wave beams, this mixing volume changes over time with the overlap region of the pulses which was numerically computed.

In Chapter 4, the previous insights were used to optimize the measurement setup and look at technical limitations.

First, an analysis of the generated wave field by means of beam profile modeling was conducted. Three types of lobes can appear, i.e., the main lobe, side lobes and grating lobes. For linear applications the appearance of grating lobes is a limiting factor. This is not the case for the presented nonlinear technique, as they can be discriminated spatially and by frequency from the to be measured resonant wave. However, the beam width, which increases with the steering angle, is a limiting factor for the measurement setup. In order to investigate the general dependencies of the beam width on other parameters, the maximum steering angle and beam width for different frequencies was calculated for a given array design. It was found, that the beam width can be decreased for higher steering angles by the use of higher frequencies, but this also increases the attenuation. Other possibilities to decrease the beam width for higher steering angles are stated in [35]. One idea is to increase the distance δ_x between the array elements, but this facilitates the generation of further grating lobes potentially degrading the measurement quality. Another one, is the increase of the number of transducer elements to decrease the beam width, but this only works to a certain extent, with $N > 32$ number of elements leading to no significant decrease anymore. Furthermore, increasing the number of elements is limited by the currently available hardware on the market and requires very expensive or currently not available equipment. As a remedy to this issue, the use of wedges to generate an offset angle by refraction was proposed. Thereby, shifting the limited range of steering angles of the phased arrays into the region of interest where the mixing conditions can be fulfilled.

Second, the influence of attenuation on the measurement principle was studied. It was found, that points on the lower ratio isogonics are subject to less overall attenuation. Due to their lower ratio a, lower frequencies for the second incident wave can be used and the

sum frequency of the resonant wave is lower as well. Additionally, points on these lines are closer to the surface with the receiver and therefore the resonant wave gets less attenuated. This result, favors the use of in plane polarized incident waves, as they generate higher resonant amplitudes in the region with $a < 2.5$.

Finally, a simulation for a circular shaped volume with increased nonlinearity was done. It was shown, that for the compensation of the dependence of the acoustic nonlinearity parameter β_{rel} on the mixing condition, a priori knowledge about the TOE of an intact specimen of the same material composition or multiple measurements of intact regions are needed.

5.2 Outlook

For future work, insights through crack and damage modeling and its influence on nonlinearity is an important research field. The development of analytical models investigating a relationship between TOE l, m, n and damage parameters like crack density and size would be of interest for damage assessment. Additionally, the influence of cracks filled with gel produced by alcali-silica reaction (ASR) on the nonlinearity could be further investigated. Furthermore, recent models for forces acting on crack surfaces could be extended to the application of shear stresses.

Concerning the herein presented measurement technique, further advances in hardware development and practical measurements with the proposed setup have to be conducted. Especially, advances in the array technology in the NDE field could lead to broader application of the hardware. Development of phased array antennae controllers using wave generators in combination with PLL circuits would lead to better performance and control to conduct measurements.

Different approaches for the modeling of the interaction volume can lead to more precise simulation. Thereby, the results for combination of the beam steering delay law with beam focusing can be predicted. Thus, potentially enabling an improvement in the scanning

resolution and intensity of the measured signal.

Another topic is the optimization of the hardware design of the phased arrays for the presented setup. Multiple parameters can be adjusted to fit for the application with different materials, e.g., metal inspection.

Section 4.4 discussed the approximate compensation for the dependency of β_{rel} on a through the TOE. Better compensation algorithms using the a priori knowledge could be developed. Computer vision techniques could be used to better identify regions with increased nonlinearity , e.g., a water shed algorithm for segmentation or a canny edge detector. Based on the size and density of these regions, machine learning algorithms could be employed to predict the lifetime and detect dangerous micro-structural damage in advance. Furthermore, the zero amplitude point for in plane polarized shear waves can be used for calibration purposes. For example, a gradient free optimization algorithm could be used to change the beam angles until a minimum is found and this information can be used for the calculation of material parameters or as a baseline calibration.

Finally, other types of mixing interactions should be analyzed, in order to evaluate their advantages and disadvantages for the measurement of the acoustic nonlinearity parameter β_{rel}.

REFERENCES

[1] P. B. Nagy. “Fatigue damage assessment by nonlinear ultrasonic materials characterization”. In: *Ultrasonics* 36.1-5 (1998), pp. 375–381.

[2] J. H. Cantrell and W. T. Yost. “Nonlinear ultrasonic characterization of fatigue microstructures”. In: *International Journal of fatigue* 23 (2001), pp. 487–490.

[3] C. Bermes et al. “Experimental characterization of material nonlinearity using Lamb waves”. In: *Applied physics letters* 90.2 (2007), p. 021901.

[4] B. W. Drinkwater and P. D. Wilcox. “Ultrasonic arrays for non-destructive evaluation: A review”. In: *NDT & e International* 39.7 (2006), pp. 525–541.

[5] C. Holmes, B. W. Drinkwater, and P. Wilcox. “The post-processing of ultrasonic array data using the total focusing method”. In: *Insight-Non-Destructive Testing and Condition Monitoring* 46.11 (2004), pp. 677–680.

[6] J. N. Potter, A. J. Croxford, and P. D. Wilcox. “Nonlinear ultrasonic phased array imaging”. In: *Physical review letters* 113.14 (2014), p. 144301.

[7] G. L. Jones and D. R. Kobett. “Interaction of elastic waves in an isotropic solid”. In: *The Journal of the Acoustical society of America* 35.1 (1963), pp. 5–10.

[8] F. R. Rollins Jr. “Interaction of ultrasonic waves in solid media”. In: *Applied Physics Letters* 2.8 (1963), pp. 147–148.

[9] Y. Zhao et al. “Detection and Characterization of Randomly Distributed Microcracks in Elastic Solids by One-Way Collinear Mixing Method”. In: *Journal of Nondestructive Evaluation* 37.3 (2018), p. 47.

[10] P. Blanloeuil, A. Meziane, and C. Bacon. “2D finite element modeling of the non-collinear mixing method for detection and characterization of closed cracks”. In: *NDT & E International* 76 (2015), pp. 43–51.

[11] L. D. Landau and E. M. Lifshitz. “Theory of elasticity”. In: *Course of theoretical physics* 7 (1970).

[12] F. D. Murnaghan. *Finite deformation of an elastic solid*. Wiley, 1951.

[13] S. Eldevik. “Measurement of non-linear acoustoelastic effect in steel using acoustic resonance”. In: (2014).

[14] A. Bedford and D. S. Drumheller. “Elastic wave propagation”. In: *John Wileg g Sons* (1994), pp. 151–165.

[15] M. F. Hamilton, D. T. Blackstock, et al. *Nonlinear acoustics*. Vol. 237. Academic press San Diego, 1998.

[16] W. S. Slaughter. *The linearized theory of elasticity*. Springer Science & Business Media, 2012.

[17] V. A. Korneev and A. Demčenko. “Possible second-order nonlinear interactions of plane waves in an elastic solid”. In: *The Journal of the Acoustical Society of America* 135.2 (2014), pp. 591–598.

[18] Z. Chen et al. “Mixing of collinear plane wave pulses in elastic solids with quadratic nonlinearity”. In: *The Journal of the Acoustical society of America* 136.5 (2014), pp. 2389–2404.

[19] M. Liu et al. “Measuring acoustic nonlinearity parameter using collinear wave mixing”. In: *Journal of applied physics* 112.2 (2012), p. 024908.

[20] A. J. Croxford et al. “The use of non-collinear mixing for nonlinear ultrasonic detection of plasticity and fatigue”. In: *The Journal of the Acoustical Society of America* 126.5 (2009), EL117–EL122.

[21] M. Sun et al. “Scanning non-collinear wave mixing for nonlinear ultrasonic detection and localization of plasticity”. In: *NDT & E International* 93 (2018), pp. 1–6.

[22] T. Ju et al. “Nondestructive evaluation of thermal aging of adhesive joints by using a nonlinear wave mixing technique”. In: *Ndt & E International* 103 (2019), pp. 62–67.

[23] T. Ju et al. “One-way mixing of collinear waves in an adhesive layer”. In: *The Journal of the Acoustical Society of America* 145.1 (2019), pp. 110–120.

[24] Z. Zhang, P. B. Nagy, and W. Hassan. “Analytical and numerical modeling of non-collinear shear wave mixing at an imperfect interface”. In: *Ultrasonics* 65 (2016), pp. 165–176.

[25] Z. Zhang, P. B. Nagy, and W. Hassan. “Numerical study of material nonlinearity assessment based on non-collinear ultrasonic wave mixing”. In: *AIP Conference Proceedings*. Vol. 1650. 1. American Institute of Physics. 2015, pp. 1599–1608.

[26] B. Mi, J. E. Michaels, and T. E. Michaels. “An ultrasonic method for dynamic monitoring of fatigue crack initiation and growth”. In: *The Journal of the Acoustical Society of America* 119.1 (2006), pp. 74–85.

[27] C. Payan et al. “Determination of third order elastic constants in a complex solid applying coda wave interferometry”. In: *Applied Physics Letters* 94.1 (2009), p. 011904.

[28] C. Payan, V. Garnier, and J. Moysan. “Determination of nonlinear elastic constants and stress monitoring in concrete by coda waves analysis”. In: *European journal of environmental and civil engineering* 15.4 (2011), pp. 519–531.

[29] Y. S. Cho and F.-B. Lin. “Spectral analysis of surface wave response of multi-layer thin cement mortar slab structures with finite thickness”. In: *NDT & E International* 34.2 (2001), pp. 115–122.

[30] W. N. Reynolds, S. J. Wilkinson, and D. C. Spooner. “Ultrasonic wave velocities in concrete”. In: *Magazine of Concrete Research* 30.104 (1978), pp. 139–144.

[31] C. Pecorari. “Modeling non-collinear mixing by distributions of clapping microcracks”. In: *Wave Motion* 59 (2015), pp. 69–80.

[32] J. Jiao et al. “Micro-crack detection using a collinear wave mixing technique”. In: *Ndt & E International* 62 (2014), pp. 122–129.

[33] V. E. Nazarov and A. M. Sutin. “Nonlinear elastic constants of solids with cracks”. In: *The Journal of the Acoustical Society of America* 102.6 (1997), pp. 3349–3354.

[34] S. Wooh and Y. Shi. “A simulation study of the beam steering characteristics for linear phased arrays”. In: *Journal of nondestructive evaluation* 18.2 (1999), pp. 39–57.

[35] S. Wooh and Y. Shi. “Optimum beam steering of linear phased arrays”. In: *Wave motion* 29.3 (1999), pp. 245–265.

[36] S. Wooh and Y. Shi. “Three-dimensional beam directivity of phase-steered ultrasound”. In: *The Journal of the Acoustical Society of America* 105.6 (1999), pp. 3275–3282.

[37] T. P. Philippidis and D. G. Aggelis. “Experimental study of wave dispersion and attenuation in concrete”. In: *Ultrasonics* 43.7 (2005), pp. 584–595.

[38] T. Ju et al. “Ultrasonic nondestructive evaluation of alkali–silica reaction damage in concrete prism samples”. In: *Materials and structures* 50.1 (2017), p. 60.